

Hydrogen Distribution in Metallic Polycrystals with Deformation

Rakesh Kumar , Dhiraj K. Mahajan

PII: S0022-5096(19)30462-4
DOI: <https://doi.org/10.1016/j.jmps.2019.103776>
Reference: MPS 103776

To appear in: *Journal of the Mechanics and Physics of Solids*

Received date: 27 May 2019
Revised date: 3 October 2019
Accepted date: 1 November 2019

Please cite this article as: Rakesh Kumar , Dhiraj K. Mahajan , Hydrogen Distribution in Metallic Polycrystals with Deformation, *Journal of the Mechanics and Physics of Solids* (2019), doi: <https://doi.org/10.1016/j.jmps.2019.103776>



This is a PDF file of an article that has undergone enhancements after acceptance, such as the addition of a cover page and metadata, and formatting for readability, but it is not yet the definitive version of record. This version will undergo additional copyediting, typesetting and review before it is published in its final form, but we are providing this version to give early visibility of the article. Please note that, during the production process, errors may be discovered which could affect the content, and all legal disclaimers that apply to the journal pertain.

Hydrogen Distribution in Metallic Polycrystals with Deformation

Rakesh Kumar, Dhiraj K. Mahajan*

Ropar Mechanics of Materials Laboratory, Department of Mechanical Engineering, Indian Institute of Technology Ropar, Rupnagar, Punjab, India, 140001

*dhiraj.mahajan@iitrpr.ac.in

Abstract

To understand hydrogen embrittlement and predict probable damage sites based on high hydrogen segregation, it is important to identify hydrogen distribution mechanisms in metallic microstructure with deformation. Hydrogen segregation in metals is affected by various factors such as grain-size, the character of grain boundaries (GBs), loading direction and strain-rate. To this end, a computational framework consisting of non-local dislocation density-based crystal plasticity model coupled with slip-rate based hydrogen transport model is presented to study the role of (i) grain-size (ii) loading direction, (iii) strain-rate and (iv) GB character on hydrogen distribution and segregation in the pre-charged metallic microstructure. The computational framework is capable of accounting for the change in local hydrogen concentration due to prevailing hydrostatic pressure, trapping by dislocations, GB energetics and local slip-rates in the metallic microstructure. The difficulty in dislocation motion at the inter-granular regions of polycrystal due to high cross-hardening offered by geometrically necessary dislocations (GNDs) is incorporated in the model as additional isotropic hardening, whereas the back stress due to the GND pileups is included as a kinematic term in the flow rule. In addition, GNDs act as hydrogen trap sites leading to increased hydrogen concentration in the inter-granular regions. The strain-rate factor initially provided by Krom & Bakker (1999) is modified in the present work to make it compatible with the dislocation density-based coupled framework, which is able to calculate trapped hydrogen in dislocations along the slip systems. Plastically deformed polycrystals of various grain-sizes, along different directions, with varying strain rates and containing $\Sigma 3[1\bar{1}0](111)$ and $\Sigma 5[001](210)$ GBs show that the gradients of hydrostatic pressure and GB character are major factors controlling hydrogen segregation in the microstructure.

1. Introduction

To establish the hydrogen-based economy and meet ambitious CO_2 emission targets, developing high strength metals that are resistant to hydrogen embrittlement (HE) is the key requirement (Paxton et al., 2017). Hydrogen embrittlement (HE) is the phenomenon of reduction in ductility, fracture toughness and increased fatigue crack-growth rate in metals due to the presence of hydrogen in their microstructure (Johnson, 1875; Murakami and Matsuoka, 2010; Robertson et al., 2015). Several atomic-scale mechanisms are proposed in the literature that explain this phenomenon through the interaction of particular microstructural features with hydrogen. For example, hydrogen enhanced localized plasticity (HELP) mechanism is associated with hydrogen-dislocation interaction leading to early damage due to decrease in the dislocation interaction energy (Beachem, 1972; Birnbaum and Sofronis, 1994), hydrogen enhanced decohesion (HEDE) mechanism is linked with high hydrogen concentration at the grain boundaries (GBs) or in front of the crack-tip that leads to decohesion of atoms caused by decrease in their cohesive energy (Lynch, 2011; Oriani R.A., 1972) and hydrogen enhanced strain-induced vacancy (HESIV) generation is linked with the reduction in the vacancy formation energy due to the presence of hydrogen in the microstructure (Fukai, 2003; Li et al., 2017; Nagumo, M., Nakamura M., 2001; Oudriss et al., 2012a; Wen et al., 2009) among others. Irrespective of these atomic-scale embrittling mechanisms, damage caused by hydrogen is associated with large scale accumulation of hydrogen atoms at the stress concentration sites within the microstructure such as GBs in a crack-free metallic specimen. Therefore, to mitigate

HE, it is necessary first to understand the factor governing hydrogen distribution and segregation in the metallic microstructure with deformation.

Hydrogen as a solute atom resides in the metallic microstructure at two sites i.e., normal interstitial lattice sites (NILS) and trap sites. Various defects sites such as dislocations (Magnin et al., 2001; Wang et al., 2013; Xie et al., 2016), vacancies (Li et al., 2017; Oudriss et al., 2012a; Wen et al., 2009; Xie et al., 2016) and grain boundaries (Oudriss et al., 2012b, 2012a) act as trap sites while NILS provide diffusion pathway for hydrogen atoms to transport freely within the microstructure. These defect sites hold hydrogen either weakly or strongly depending on their binding energy (Di Stefano et al., 2015; Kumnick and Johnson, 1980; Pressouyre, 1979) and the equilibrium between the occupancies of NILS and defect sites controls the hydrogen segregation at the critical sites (such as GBs) in the microstructure prone to HE (Oriani R.A., 1970).

Deformation assisted hydrogen distribution and segregation in the microstructure is affected by microstructural factors such as grain-size and crystallographic character of GBs (such as random or special GBs e.g. $\Sigma 3[1\bar{1}0](111)$ or $\Sigma 5[001](210)$ where the numeric value followed by “ Σ ” represents the reciprocal coincident site lattice density along the GB, the Miller indices in square brackets represents the misorientation axis and round brackets represents the GB plane between the two neighbouring grains) as well as external factors such as loading direction with respect to GB plane and the rate of deformation. Grain-size dependent transition in HE mechanisms is often reported in literature where HEDE is observed in the coarse-grained samples due to increased hydrogen segregation at GBs and HELP is predominant in the fine-grained samples due to enhanced hydrogen-dislocation interaction in the microstructure (Chen et al., 2014; Oudriss et al., 2012a; Park et al., 2017; Takasawa et al., 2011; Zan et al., 2015). Likewise, the crystallographic character of GBs controls the hydrogen segregation at the inter-granular region either due to variation in their atomic structure that can lead to GBs acting as a strong or weak trap (Di Stefano et al., 2015; Tehranchi and Curtin, 2017); or due to variation in the evolution of dislocations linked hydrogen segregation in the inter-granular regions of the microstructure depending on the plastic inhomogeneities generated between the neighbouring grains with deformation (Oudriss et al., 2012b, 2012a). Under such scenario, multiple HE mechanisms driven by hydrogen-dislocation and hydrogen-GB interaction may operate simultaneously e.g., the synergistic action of HEDE and HELP at GBs as reported in the literature (Djukic et al., 2019, 2015; Novak et al., 2010; Singh et al., 2019).

Among the external factors, loading direction with respect to the GB plane can affect hydrogen segregation at the intra- and inter-granular regions of the polycrystals caused by variation in the evolution of dislocation density as well as gradient of hydrostatic pressure in these regions (Jun et al., 2018; Liu and Hansen, 1995; Lu et al., 2017). Similarly, the rate of deformation also affects the distribution and segregation of hydrogen in the microstructure showing transition in the fracture process of hydrogen charged specimens from ductile and trans-granular failure in case of high strain rate deformation to quasi-cleavage and inter-granular in case of slow strain rate deformation (Bal et al., 2016; Doshida and Takai, 2014; Kubin and Estrin, 1991; Kwon et al., 2018; Momotani et al., 2017; Murakami and Matsuoka, 2010). Understanding the importance of these microstructural and external factors on hydrogen distribution in the metals holds the key for identifying the high hydrogen segregation sites in their microstructure. Based on this understanding, designing a metallic microstructure that can control the presence of such sites will eventually help in developing new HE resistant metals. Since it is difficult to track the embrittling effect of hydrogen in metals experimentally, a comprehensive computation framework able to incorporate the above-mentioned factors is desirable to elucidate their synergetic role on hydrogen distribution and segregation in the metallic microstructures.

A computational framework that can model the hydrogen diffusion-deformation coupled problem is required for this purpose. Several such frameworks exist in the literature that can simulate hydrogen-metal interaction at different length scales. For example, atomic-scale simulations are

regularly used to provide insights into the various HE mechanisms (HEDE, HELP, etc.) at the single crystal as well as polycrystal levels (Tehranchi and Curtin, 2019). These simulations highlight the effect of hydrogen on dislocation nucleation (Song and Curtin, 2012; Wen et al., 2009; Zhou et al., 1998), interaction (Itakura et al., 2013; Lu et al., 2001), mobility (Itakura et al., 2013; Paxton and Katzarov, 2016; Song and Curtin, 2014) as well as propensities of GBs to hydrogen segregation (Di Stefano et al., 2015; Tehranchi and Curtin, 2017). At the dislocation dynamics scale, discrete dislocation dynamics (DDD) simulations of dislocation-hydrogen interactions are performed in greater detail with a focus on understanding the HELP mechanism in different metals (Gu and El-awady, 2018; Yu et al., 2018). These small-scale simulations are essential to gain fundamental insights into the individual HE mechanisms. However, the length scale that can be simulated using either atomistic or DDD simulations puts a limit on understanding the synergistic role of various microstructural and external factors affecting the hydrogen distribution and segregation in metals, as discussed earlier. For this reason, physics-based continuum scale computational frameworks are an ideal choice for modelling the hydrogen-metal interaction in realistic microstructures at larger scales.

Among the continuum scale modeling frameworks, Sofronis and McMeeking (1989) were the first ones to report a hydrogen diffusion-deformation coupled framework to simulate the hydrogen distribution at the front of a blunting crack tip. The hydrogen transport model that was implemented into the finite element framework accounts for the equilibrium of hydrogen in NILs and trap sites (Oriani R.A., 1970). However, the total hydrogen concentration in their model was not balanced due to the continuous creation of trap hydrogen with deformation against a constant lattice hydrogen concentration, which otherwise should decrease at a material point with deformation due to subsequently filling of trap sites by hydrogen. Krom et al. (1999) provided a solution to this issue in the coupled framework by introducing a strain-rate factor in the hydrogen transport model. The strain-rate factor was shown to provide a balance of total hydrogen concentration with the hydrogen in NILS and trap sites under deformation. These continuum scale frameworks that consider classical plasticity only provide limited information on hydrogen-dislocation interaction in the metallic specimens. To overcome this, Martínez-Pañeda et al. (2016a, 2016b) implemented a phenomenological and mechanism-based strain gradient-based plasticity model in the hydrogen diffusion-displacement coupled framework to account for the diffusible hydrogen field at the blunting crack tip. With the help of these advance plasticity models, the prominent role of geometrically necessary dislocations (GNDs) with respect to statistically stored dislocations (SSDs) was highlighted in the local strengthening of the material. These physics-based continuum level computational frameworks, however, still cannot account for the synergistic role of microstructural and external factors on hydrogen distribution due to lack of microstructural information. For this reason, the hydrogen diffusion-displacement coupled framework using the crystal plasticity model is desirable. In this direction, Hassan et al. (2018) using a one-way coupled model of phenomenological crystal plasticity and hydrogen transport model showed the effect of hydrostatic pressure and residual stresses on the distribution of hydrogen in a virtual polycrystal microstructure with deformation. However, due to the local crystal plasticity model used in their framework, the effective role of microstructural and external factors cannot be accounted for accurately. Thus, a non-local physics-based crystal plasticity model that can account for the segregation of total dislocation density into SSD density (ρ_{SSD}) and GND density (ρ_{GND}) is desirable in such a coupled framework.

In this paper, a one-way coupled non-local dislocation density-based crystal plasticity model with a slip-rate based hydrogen transport model is presented to elucidate the synergetic role of grain-size, the crystallographic character of GBs, loading direction with respect to grain boundary plane and strain-rate on hydrogen distribution in metallic microstructure with deformation. Due to one-way coupling, hydrogen distribution and segregation in the microstructure is modulated by the evolution of dislocation plasticity and stress distribution with deformation while the effect of hydrogen on dislocation plasticity and stress distribution is not considered. In addition, the GBs between two

grains are considered as an impenetrable obstacle to dislocations. The strain-rate factor, as proposed by Krom et al. (1999) used in the hydrogen transport model is modified in the present work to make it compatible with the non-local dislocation density-based crystal plasticity model. The modified factor is able to consider local slip-rates that are affected by the local evolution of ρ_{SSD} and ρ_{GND} with deformation in the metallic microstructures. This factor is capable of resolving slip-rate dependent trapped hydrogen concentration along the slip systems at a material point. Representative volume elements (RVE) consisting of three-grain polycrystal with controlled grain-size, orientations and fixed initial hydrogen concentration throughout the polycrystal is used to study the hydrogen distribution in the polycrystal with deformation. A comparison of the non-local model with the local model is also presented to elucidate the role of non-local terms to correctly account for factors controlling the hydrogen distribution in the microstructure.

The paper is organized as follows. In the next section, we explain the proposed micromechanical modelling framework consisting of a dislocation density-based crystal plasticity model and a slip-rate based hydrogen transport model along with the coupling scheme and numerical aspects. In Section 3, the application of the proposed framework to study the effect of grain-size, loading direction, strain-rate and GB character on hydrogen distribution and segregation in the polycrystal is presented. Section 4 discusses the results followed by the conclusions drawn from this work in Section 5.

2. Modelling framework

The proposed non-local dislocation density-based crystal plasticity model segregates total dislocation density into ρ_{SSD} and ρ_{GND} at a material point in the simulated microstructure. Incorporation of GNDs in the crystal plasticity framework accounts for crystallographic mismatch at the GBs as well as the size effect shown by metallic material caused by reduced grain-size (Meissonnier et al., 2001). The hydrogen concentrations at NILS and trap sites, on the other hand, are calculated using slip-rate based hydrogen transport model. The capabilities of the framework to simulate the effects of grain size, strain rate and loading direction are first shown by considering only dislocation as primary trapping sites while the GBs act as physical obstruction for dislocation gliding from one grain to another. The effect of the crystallographic character of GB on hydrogen distribution and segregation in the microstructure is incorporated by including GB specific properties such as diffusivity and trap binding energies in this framework, as explained in section 3.4. The modelling framework is presented in the following subsections in which bold letters represent the tensor quantities; non-bold letters represent scalars and $(.)_{ij}$ is the indicial representation of tensor quantities.

2.1. Dislocation density-based crystal plasticity model

A non-local dislocation density-based crystal plasticity model is developed in this work. In this model, multiplicative decomposition of deformation gradient, \mathbf{F} as

$$\mathbf{F} = \mathbf{F}^e \mathbf{F}^p \quad (1)$$

is used to model the kinematics of deformation, where \mathbf{F}^e and \mathbf{F}^p are elastic and plastic part of the deformation gradient. The plastic deformation gradient rate, $\dot{\mathbf{F}}^p$ in the current time step, is calculated by multiplying the plastic velocity gradient, \mathbf{L}^p with the previous time step \mathbf{F}^p as

$$\dot{\mathbf{F}}^p = \mathbf{L}^p \mathbf{F}^p \quad (2)$$

with \mathbf{L}^p given as

$$\mathbf{L}^p = \sum_{\alpha=1}^N \dot{\gamma}^{\alpha} (\mathbf{m}^{\alpha} \otimes \mathbf{n}^{\alpha}) \quad (3)$$

In the equation (3), $N = 12$ as face-centred cubic (fcc) metal nickel is considered for simulations, $\mathbf{m}^{\alpha} \otimes \mathbf{n}^{\alpha}$ defines the Schmid matrix where \mathbf{m}^{α} and \mathbf{n}^{α} are orthonormal unit vector defined as slip

direction and slip plane normal for α slip system, while \otimes represents the dyadic product. Second Piola Kirchhoff stress, \mathbf{S} in the intermediate configuration in terms of \mathbf{F}^e is given as

$$\mathbf{S} = \mathfrak{S} : \left(\frac{\mathbf{F}^{eT} \mathbf{F}^e - \mathbf{I}}{2} \right) \quad (4)$$

where \mathfrak{S} is fourth order anisotropic elastic stiffness tensor. The resolved shear stress is determined in the intermediate configuration by scalar operating the \mathbf{S} with Schmid matrix as

$$\tau^\alpha = \mathbf{S} \cdot (\mathbf{m}^\alpha \otimes \mathbf{n}^\alpha) \quad (5)$$

The Cauchy stress ($\boldsymbol{\sigma}$) in the current configuration is calculated using push forward approach as

$$\boldsymbol{\sigma} = \det\{\mathbf{F}^e\}^{-1} \mathbf{F}^e \mathbf{S} \mathbf{F}^{eT} \quad (6)$$

2.1.1 Evolution of Total Dislocation Density

In this model, total dislocation density (ρ^α) along any slip system α at a material point is considered as the sum of SSD density, ρ_{SSD}^α and GND density, ρ_{GND}^α . The evolution of ρ_{SSD}^α is governed by dislocation multiplication and annihilation of random encounters between dislocations as proposed by Mecking and Kocks (1981). For a slip system α , the SSD evolution rate is considered as

$$\dot{\rho}_{SSD}^\alpha = (c_1 \sqrt{\rho^\alpha} - c_2 \rho^\alpha) |\dot{\gamma}^\alpha| \quad (7)$$

where terms c_1 and c_2 govern the dislocation multiplication and annihilation on the slip system α . The evolution of GNDs is incorporated by calculating plastic strain gradients due to deformation heterogeneities in microstructure, such as caused by GBs. The GND density tensor \mathbf{G} is calculated as classical Nye tensor (Nye, 1953) given by curl of \mathbf{F}^p as

$$\mathbf{G} = -(\mathbf{F}^p \times \nabla) \quad (8)$$

The \mathbf{G} defines the closure failure of Burgers circuit with the net Burgers vector $\bar{\mathbf{b}}$. The net Burgers vector $\bar{\mathbf{b}}$ can be determined by resolving \mathbf{G} over an arbitrary unit area with normal vector $\bar{\mathbf{n}}$ as

$$\bar{\mathbf{b}} = \mathbf{G} \bar{\mathbf{n}} \quad (9)$$

The \mathbf{G} when divided by the magnitude of Burgers vector, b provides the sum total crystallographic GND density (ρ_{GND}^α) given as the sum of edge part (ρ_{GNDe}^α) and screw part (ρ_{GNDs}^α) of GNDs along slip-system α at a given material point as

$$\sum_{\alpha=1}^N \rho_{GNDe}^\alpha (\mathbf{m}^\alpha \otimes \mathbf{t}^\alpha) + \sum_{\alpha=1}^N \rho_{GNDs}^\alpha (\mathbf{m}^\alpha \otimes \mathbf{m}^\alpha) = \frac{1}{b} \mathbf{G} \quad (10)$$

where $\mathbf{t}^\alpha = \mathbf{m}^\alpha \times \mathbf{n}^\alpha$ is the dislocation line vector. The presence of GNDs contributes to increased strength at a given material point. The gradient of GNDs i.e., second gradient of \mathbf{F}^p at a material point on the other hand, signifies the pileup of GNDs. Increased strength is associated with isotropic hardening, whereas pileup of GNDs causes a back stress that leads to kinematic hardening at a material point (Ma and Hartmaier, 2014).

2.1.2 Isotropic hardening due to GNDs

The forest GNDs provide cross-hardening to the crystallographic mobile dislocations. The hardening offered by GNDs is calculated as Taylor hardening leading to additional passing stress for mobile dislocations as

$$\tau_{GNDi}^\alpha = \left(c_3 \mu b \sqrt{\sum_{\beta=1}^N \chi_{\alpha\beta} \rho_{GND}^\beta} \right) \quad (11)$$

where c_3 is the Taylor hardening coefficient, μ is shear modulus of the material. The cross-hardening matrix, $\chi_{\alpha\beta}$ includes the effect of self-hardening and latent hardening of mobile dislocation due to GNDs respectively through diagonal and non-diagonal elements respectively.

2.1.3 Kinematic hardening due to pileup of GNDs

The presence of a gradient of GNDs in the material signifies a dislocation pileup that leads to back-stress associated with it. By resolving the nine components of \mathbf{G} along twelve slip systems in the case of fcc metals does not guarantee a unique solution (Meissonnier et al., 2001). Therefore, to calculate the accurate back stress (i.e., kinematic hardening) along the different slip systems at a material point, \mathbf{G} is resolved along nine independent parts with the help of three mutually perpendicular global coordinate axes \mathbf{e}_1 , \mathbf{e}_2 and \mathbf{e}_3 (Ma and Hartmaier, 2014). The GNDs that we get through this procedure are called super GNDs and are used to calculate the back stress due to GND pileup. This method leads to a better approximation of far-field stresses present in the microstructure that are important for this work. The gradient of super GNDs can be calculated by resolving \mathbf{G} along global coordinate axes, i as

$$\bar{\rho}_{GND,i}^\delta = \frac{1}{b} G_{jk,i} \bar{m}_j^\delta \bar{t}_k^\delta. \quad (12)$$

where δ varies from 1 to 9, $\bar{\mathbf{m}}^\delta$ is the super GND Burger vector direction and $\bar{\mathbf{t}}^\delta$ is super GND line direction. At a material point at η with a small neighbourhood volume L^3 , the net Burgers vector along δ , $(\Delta \bar{\mathbf{b}}_i^\delta)$ is calculated as

$$\Delta \bar{\mathbf{b}}_i^\delta = \frac{1}{2} (\bar{\rho}_{GND,i}^\delta L^3) \bar{\mathbf{m}}^\delta. \quad (13)$$

The back stress due to super GND pileup is approximated by the stress field of a single dislocation segment, representing the pileup, with fixed start and end points in the neighbourhood of the given material point, as defined by Devincere (1995), and implemented in non-local crystal plasticity model by Ma and Hartmaier (2014). For a material point at η , the starting point $\bar{\xi}_i^\delta$ and end point $\bar{\zeta}_i^\delta$ of each single dislocation segment is calculated as

$$\bar{\xi}_i^\delta = \eta + \frac{L}{4} \mathbf{e}_i + \frac{L}{2} \bar{\mathbf{t}}^\delta \text{ and } \bar{\zeta}_i^\delta = \eta + \frac{L}{4} \mathbf{e}_i - \frac{L}{2} \bar{\mathbf{t}}^\delta$$

Using $\Delta \bar{\mathbf{b}}_i^\delta$, the back stress, \mathbf{S}_{GND} from a super GND pileup is approximated by the standard stress field of a single dislocation segment in an isotropic elastic material (Devincere, 1995; Ma and Hartmaier, 2014) at the reference configuration as

$$\mathbf{S}_{GND} = \sum_{\delta=1, i=1}^{9,3} \mathbf{C}(\eta, \bar{\xi}_i^\delta, \bar{\zeta}_i^\delta) \Delta \bar{\mathbf{b}}_i^\delta \quad (14)$$

where $\mathbf{C}(\eta, \bar{\xi}_i^\delta, \bar{\zeta}_i^\delta)$ is a third-order tensor for a single dislocation segment. The back stress in the intermediate configuration, $\bar{\mathbf{S}}_{GND}$ caused by the super GND pileup is given by

$$\bar{\mathbf{S}}_{GND} = \mathbf{F}^P \mathbf{S}_{GND} \mathbf{F}^{PT} \quad (15)$$

The kinematic hardening or back stress (τ_{GNDk}^α) on α slip system is then resolved by operating the $\bar{\mathbf{S}}_{GND}$ with Schmid matrix as

$$\tau_{GNDk}^\alpha = \bar{\mathbf{S}}_{GND} \cdot (\mathbf{m}^\alpha \otimes \mathbf{n}^\alpha) \quad (16)$$

2.1.4 Flow rule and hardening law for non-local dislocation density-based CP model

The $\dot{\gamma}^\alpha$ is the slip-rate along α slip system and is defined by using classical Orowan-law (E Orowan, 1940) as

$$\dot{\gamma}^\alpha = \rho^\alpha b v^\alpha$$

where v^α is dislocation velocity along α slip system which is a function of resolved shear stress τ^α , the critical resolved shear stress τ_c^α , strain-rate sensitivity n and reference velocity v_0 (Engels et al., 2012). The back stress due to dislocation pileup provides an additional contribution to the resolved shear stress τ^α such that the slip-rate can be written as

$$\dot{\gamma}^\alpha = \rho^\alpha b v_0 \left| \frac{\tau^\alpha + \tau_{GNDk}^\alpha}{\tau_c^\alpha} \right|^n \text{sgn}(\tau^\alpha) \quad (17)$$

The SSDs and GNDs (refer eq. (7) and (10)), on the other hand, contribute to the hardening evolution of slip systems expressed by the Taylor rule as

$$\tau_c^\alpha = c_3 \mu b \sqrt{\sum_{\beta=1}^N \chi_{\alpha\beta} \left(\rho_{SSD}^\beta + \rho_{GND}^\beta \right)} \quad (18)$$

2.2. Slip-rate based hydrogen transport model

Hydrogen in metals is categorised based on its occurrence at two sites namely NILS giving hydrogen concentration as C_L and trap sites giving the trapped part of hydrogen concentration as C_T . As dislocations are the primary trap sites considered in the present work, the hydrogen concentration along α slip system is denoted by C_T^α . The total hydrogen concentration C_{Tot} in the material can then be given as

$$C_{Tot} = C_L + \sum_{\alpha} C_T^\alpha \quad (19)$$

As only C_L is considered responsible for hydrogen diffusion in material, the chemical potential (μ_L) of lattice hydrogen in a body under the influence of hydrostatic pressure, ($\sigma_H = -\frac{1}{3} \sum_{i=1}^3 \sigma_{ii}$) is given as

$$\mu_L = \mu_{L0} + RT \ln \frac{C_L}{N_L} + \bar{V}_H \sigma_H \quad (20)$$

where μ_{L0} is the chemical potential of hydrogen at a reference temperature and pressure, \bar{V}_H is the partial molar volume of hydrogen in nickel, R is universal gas constant and T is temperature. When the evolution of total hydrogen concentration in an enclosed volume dV of a metallic microstructure is equal to the net flux, \mathbf{J} , of the hydrogen at the surface with unit normal vector $\hat{\mathbf{n}}$ and surface area dA , the mass conservation equation can be written as

$$\int \{C_L + \sum C_T^\alpha\} dV + \int \mathbf{J} \cdot \hat{\mathbf{n}} dA = 0 \quad (21)$$

The hydrogen flux through the surface is given by

$$\mathbf{J} = -M_L C_L \nabla \mu_L \quad (22)$$

Where M_L is the mobility of hydrogen in lattice sites. Using eq. (20) and lattice diffusivity, $D_L = \frac{M_L RT}{C_L}$, and

$$\mathbf{J} = -D_L \nabla C_L - \frac{D_L C_L \bar{V}_H}{RT} \nabla \sigma_H \quad (23)$$

where D_L is lattice diffusivity of hydrogen atoms and ∇C_L is the gradient of C_L . The effect of the gradient of hydrostatic pressure, $\nabla \sigma_H$ on hydrogen diffusion is also incorporated in eq. (23). By incorporating eq. (23) in eq. (21), the mass conservation equation can be expressed as

$$\frac{\partial C_L}{\partial t} + \sum_{\alpha} \frac{\partial C_T^\alpha}{\partial t} - \nabla \cdot (D_L \nabla C_L) - \nabla \cdot \left(\frac{D_L C_L \bar{V}_H}{RT} \nabla \sigma_H \right) = 0 \quad (24)$$

The hydrogen concentrations in lattice and trap sites are related to the total available lattice and trap sites, respectively. With the occupancy of hydrogen atoms in lattice sites (θ_L) and the occupancy of hydrogen in dislocations at α slip plane (θ_T^α), the following relationships hold at any material point

$$C_L = \theta_L N_L \quad (25)$$

and

$$C_T^\alpha = \theta_T^\alpha N_T^\alpha \quad (26)$$

where $\sum_{\alpha=1}^N C_T^\alpha = C_T$ is the total trap hydrogen concentration at a material point. With α as lattice parameter, N_T^α is the total number of traps along α slip system in fcc material (Dadfarnia et al., 2014) expressed as

$$N_T^\alpha = \frac{\sqrt{3}\rho^\alpha}{a} \quad (27)$$

The equilibrium between the occupancies of the hydrogen atom in lattice and trap sites is given by Oriani R.A. (1970). In the present work, it is assumed that the distribution of hydrogen between the lattice sites and dislocation cores lying along particular slip systems could be achieved by using the standard Oriani equilibrium. The total trapped hydrogen concentration at a material point then becomes the cumulative sum of the trapped hydrogen on total dislocations lying along all the slip systems. Using trap binding energy W_B and equilibrium constant $K_T = \exp\left(\frac{-W_B}{RT}\right)$, the following relationship holds

$$\frac{\theta_T^\alpha}{(1-\theta_T^\alpha)} = \frac{\theta_L}{(1-\theta_L)} K_T \quad (28)$$

Using eq. (28), hydrogen concentration on α slip systems can be calculated using the following relationship

$$C_T^\alpha = \frac{\theta_L N_T^\alpha K_T}{(1-\theta_L) + K_T \theta_L} \quad (29)$$

Kumnick and Johnson (1980) showed the experimental evolution of traps density with deformation for α -iron, which in this work is modelled as the evolution of SSDs and GNDs with deformation. Using the approach defined by Krom et al. (1999), the partial derivative of the trap hydrogen concentration with respect to time is defined as

$$\frac{\partial C_T^\alpha}{\partial t} = \frac{\partial C_T^\alpha}{\partial C_L} \frac{\partial C_L}{\partial t} + \frac{\partial C_T^\alpha}{\partial N_T^\alpha} \frac{\partial N_T^\alpha}{\partial \rho^\alpha} \frac{\partial \rho^\alpha}{\partial \gamma^\alpha} \dot{\gamma}^\alpha \quad (30)$$

Using $\frac{\partial C_T^\alpha}{\partial C_L} = \frac{C_T^\alpha(1-\theta_T^\alpha)}{C_L}$ and $\frac{\partial C_T^\alpha}{\partial N_T^\alpha} = \theta_T^\alpha$ through eq. (26) and (29), the eq. (30) can be written as

$$\frac{\partial C_T^\alpha}{\partial t} = \frac{C_T^\alpha(1-\theta_T^\alpha)}{C_L} \frac{\partial C_L}{\partial t} + \theta_T^\alpha \frac{\partial N_T^\alpha}{\partial \rho^\alpha} \frac{\partial \rho^\alpha}{\partial \gamma^\alpha} \dot{\gamma}^\alpha \quad (31)$$

Putting this equation in the mass conservation equation (24), a slip-rate dependent hydrogen transport model is given as

$$\frac{C_L + \sum_{\alpha=1}^N (C_T^\alpha(1-\theta_T^\alpha))}{C_L} \frac{\partial C_L}{\partial t} - \nabla \cdot (D_L \nabla C_L) - \nabla \cdot \left(\frac{D_L C_L V_H}{RT} \nabla \sigma_H \right) + \sum_{\alpha=1}^N \left(\theta_T^\alpha \frac{\partial N_T^\alpha}{\partial \rho^\alpha} \frac{\partial \rho^\alpha}{\partial \gamma^\alpha} \dot{\gamma}^\alpha \right) = 0 \quad (32)$$

The last term in the hydrogen transport model is slip-rate factor (SRF) which allow maintaining the balance in C_{Tot} (see eq. (19)) by facilitating a corresponding reduction in C_L due to the high evolution rate of traps and subsequent hydrogen filling leading to rise in C_T . In order to make a unified model capable of considering the role of grain-size, loading direction, strain-rate and GB character on hydrogen distribution in the microstructure with deformation, the strain-rate factor used in earlier hydrogen transport models (Barrera et al., 2016; Hassan et al., 2018; Krom et al., 1999) is replaced with SRF.

It is well established that with a rise in trapped hydrogen concentration, the available hydrogen for lattice diffusion decreases, consequently decreasing the diffusivity of material (Oriani R.A., 1970).

To incorporate this effect in the hydrogen transport model, a formulation originally given by Oriani R.A. (1970) is modified here to make it workable with a dislocation density-based crystal plasticity framework. The apparent diffusivity, D_{app} in the slip-rate based hydrogen transport model, is the reduced lattice hydrogen diffusivity, D_L by hydrogen fraction trapped in dislocations, given as

$$D_{app} = \frac{D_L}{\left(\frac{c_L + \sum_{\alpha=1}^N (c_T^{\alpha} (1 - \theta_T^{\alpha}))}{c_L} \right)} \quad (33)$$

The proposed coupled framework of dislocation density-based crystal plasticity and slip-rate dependent hydrogen transport model is thus able to consider the effects of trapping, hydrostatic pressure gradient and slip-rate on the distribution of hydrogen in microstructure with deformation.

2.3. Coupling scheme and numerical aspects

A weak coupling scheme is used to numerically solve the proposed one-way coupled framework of dislocation density-based crystal plasticity model and slip-rate based hydrogen transport model with the help of UMAT and UMATHT subroutines respectively in the commercial finite element solver ABAQUS. Various gradient terms in the coupled framework are calculated using the gradients of shape functions, which necessitate the use of a quadratic element type. Presently, C3D20T elements are used to generate the finite element mesh. \mathbf{F}^p and σ_H are considered as an additional degree of freedom in the proposed framework and their values at the previous converged time increment are averaged at the nodes using python script at the beginning of new time increment. The gradient of hydrostatic pressure, slip-rates along slip systems and other derivatives (e.g., $\frac{\partial N_T^{\alpha}}{\partial \rho^{\alpha}}$ and $\frac{\partial \rho^{\alpha}}{\partial \gamma^{\alpha}}$ used in eq. (32)) are then provided to UMATHT to solve the slip-rate based hydrogen transport model and provide hydrogen distribution in the current time increment.

The role of various microstructural and external factors on hydrogen distribution and segregation in the microstructure, deformation simulations of three-grain virtual polycrystal specimens of nickel with height h , as shown in the schematic in Fig. 1, are performed. A mesh with ten elements/grain along the length direction and one element each along the thickness and width directions is used for all simulations after performing a mesh sensitivity study to ensure that various gradients and properties calculated based on them are appropriately resolved. As shown in Fig. 1, the orientation of grain 3 is kept similar to grain 1 such that two similar types of GBs are formed between the adjacent grains in the polycrystals. Two particular types of special GBs i.e., $\Sigma 3[1\bar{1}0](111)$ or $\Sigma 5[001](210)$, termed hereafter as $\Sigma 3$ and $\Sigma 5$ respectively, are studied in this work. The orientations as shown in Fig. 1 for grain 1, 2 and 3, lead to the formation of $\Sigma 3$ type special GB. Hydrogen diffusivity and binding energy for these GBs are derived from the work of Di Stefano et al., (2015). Various parameters related to crystal plasticity and hydrogen transport model used in this study are given in Table 1 and Table 2, respectively. All simulations are performed with periodic boundary conditions to ensure the conformity of the displacement and additional degree of freedoms i.e., \mathbf{F}^p and σ_H at the nodes of opposite edges of the virtual polycrystal along the x -, y - and z - directions. For all plots, the variation in field variables is shown with respect to normalized length which is the length of the polycrystal divided by itself at the end of deformation.

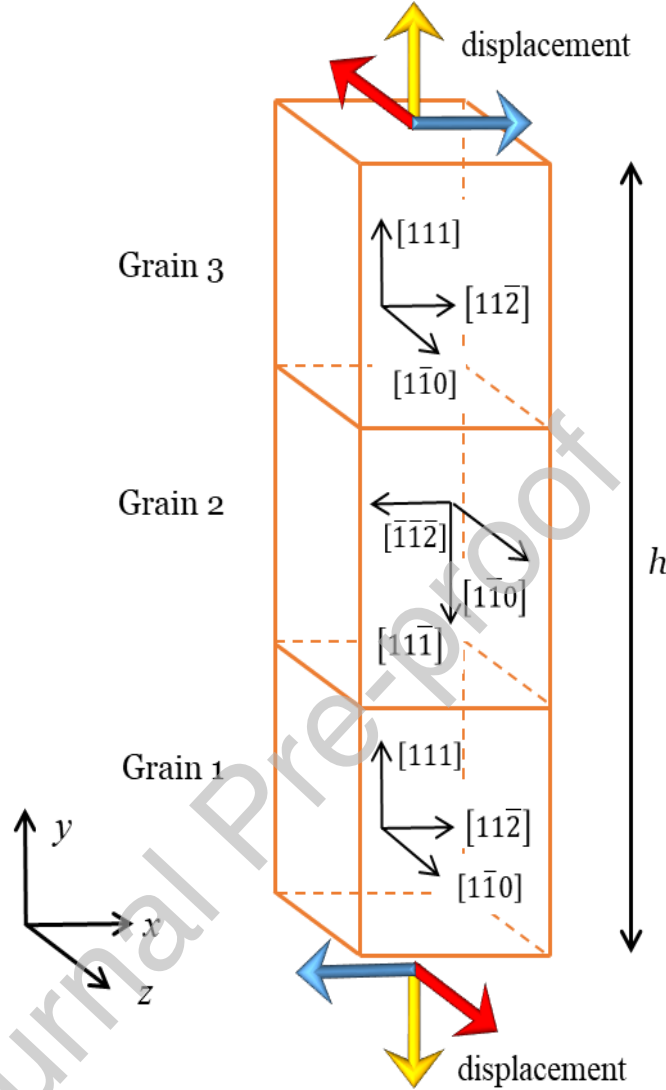


Figure 1: A schematic of a three-grain nickel polycrystal used for simulations. Schematic shows the grain orientations chosen to form two $\Sigma 3[1\bar{1}0](111)$ type GBs in the simulated polycrystal. The arrows on the top and bottom face of the polycrystal represent the direction of deformation with respect to GB plane to impose shear along x - and z -direction (as shown by violet and red colour arrows, respectively) and tensile deformation along y -direction (as shown by yellow colour arrow) to the polycrystal. Periodic boundary condition along the x -, y - and z -directions for displacement and additional degree of freedoms i.e. F^p and σ_H ensures conformity of opposite edges with deformation.

Table 1: Crystal plasticity model parameters

Parameter	Symbol	Magnitude	Units	Reference
Elastic constant	C_{11}	282	GPa	(Hachet et al., 2018)
Elastic constant	C_{12}	157	GPa	(Hachet et al., 2018)
Elastic constant	C_{44}	133	GPa	(Hachet et al., 2018)
Inverse of strain rate sensitivity	n	20	—	(Ma and Hartmaier, 2014)
Burger vector length	b	2.49×10^{-7}	mm	-
Initial dislocation density	ρ_{SSD0}	1.0×10^8	mm^{-2}	(Engels et al., 2012)
Referential dislocation velocity	v_0	5	mm/s	(Engels et al., 2012)
SSD creation parameter	c_1	$0.1/b$	—	(Engels et al., 2012)
SSD annihilation parameter	c_2	10	—	(Engels et al., 2012)
Taylor hardening parameter	c_3	0.5	—	(Engels et al., 2012)
Average dislocation pileup size	L	5×10^{-5}	mm	(Feaugas and Haddou, 2007)
Slip systems	N	12	-	-
Cross-hardening matrix	$\chi_{\alpha\beta}$	1	-	(Ma and Hartmaier, 2014)

Table 2: Hydrogen transport model parameters

Parameter	Symbol	Magnitude	Units	Reference
Number of lattice sites	N_L	1.52×10^{-4}	$\text{mol}/\text{mm}^{-3}$	-
Dislocation binding energy in nickel	W_B^{dis}	-1.0×10^7	N.mm/mol	(Angelo et al., 1995)
Initial lattice hydrogen concentration	C_{L0}	6.92×10^{-12}	$\text{mol}/\text{mm}^{-3}$	(Hachet et al., 2018)
Hydrogen diffusivity	D_L	6.0×10^{-8}	mm^2/s	(Li et al., 2017)
Partial molar volume of H in Ni	V_H	2000	mm^3	(Li et al., 2017)
Temperature	T	300	K	-
Lattice parameter	a	3.52×10^{-7}	mm	-
Gas constant	R	8314	N.mm/(mol.K)	-
$\Sigma 3$ GB diffusivity	$D_{GB}^{\Sigma 3}$	5.26×10^{-11}	mm^2/sec	(Di Stefano et al., 2015)
$\Sigma 3$ GB binding energy	$W_B^{\Sigma 3}$	-9.65×10^5	N.mm/mol	(Di Stefano et al., 2015)
$\Sigma 5$ GB diffusivity	$D_{GB}^{\Sigma 5}$	5.6×10^{-6}	mm^2/sec	(Di Stefano et al., 2015)
$\Sigma 5$ GB binding energy	$W_B^{\Sigma 5}$	-2.6×10^7	N.mm/mol	(Di Stefano et al., 2015)

3 Results

3.1 Effect of grain-size on hydrogen distribution in polycrystals

In this section, the effect of grain-size on hydrogen distribution in polycrystal with deformation is studied. The variation in the evolution of dislocation densities with respect to grain size and the corresponding hydrogen accumulation in the intra- and inter-granular regions of the polycrystal is investigated. Three three-grain virtual nickel polycrystal specimens, as shown in Fig. 1, with a grain-size of 10, 50 and 100 microns each (making the total height, h of polycrystals 30, 150 and 300 microns respectively) are used for simulations in this study. The specimens are deformed under shear strain along the x -direction (up to $\gamma_{yx} = 0.33$) by applying equal displacements on the top and bottom nodes at a constant strain rate of $3.3 \times 10^{-4} \text{ s}^{-1}$. Normalized results shown in this section are plotted after the end of the deformation.

The intra-granular regions show large deformation compared to inter-granular regions leading to increased ρ_{SSD} , whereas, plastic strain heterogeneity at GBs leads to a sharp rise in ρ_{GND} in the inter-granular region. With decreasing grain-size, ρ_{SSD} and ρ_{GND} increase in the intra-granular and inter-granular regions, respectively. The evolution of SSD densities ($\rho_{SSD}/\rho_{SSD0} = \sum_{\alpha=1}^N \rho_{SSD}^{\alpha} / \rho_{SSD0}$) and GND densities ($\rho_{GND}/\rho_{SSD0} = \sum_{\alpha=1}^N \rho_{GND}^{\alpha} / \rho_{SSD0}$) in the intra- and inter-granular regions of the polycrystals as a function of grain-size is shown in Fig. 2(a) and Fig. 2(b), respectively. A strong heterogeneity in the plastic strain at GBs leads to a sharp jump in various

quantities calculated using gradients of \mathbf{F}^P in inter-granular region. The jump in the ρ_{SSD} from one grain to another at the GB is similar for all three polycrystals, whereas, the jump in ρ_{GND} at the GB is amplified for the smallest grain polycrystal. This leads to significant jumps in both deformation and diffusion related quantities at the GBs for the smallest grain size polycrystal. The strong evolution of GNDs at the inter-granular region led to the evolution of additional isotropic ($\tau_{GNDi} = \sum_{\alpha=1}^N |\tau_{GNDi}^{\alpha}|$) as well as kinematic ($\tau_{GNDk} = \sum_{\alpha=1}^N |\tau_{GNDk}^{\alpha}|$) hardening. While τ_{GNDi} depends on the first gradient of \mathbf{F}^P (see eq. (8)), τ_{GNDk} is dependent on the second gradient of \mathbf{F}^P (see eq. (13)) which is strongest at the inter-granular region. The variation of τ_{GNDi} and τ_{GNDk} in the intra- and inter-granular regions of the polycrystals with grain size is shown in Fig. 2(c) and Fig. 2(d), respectively.

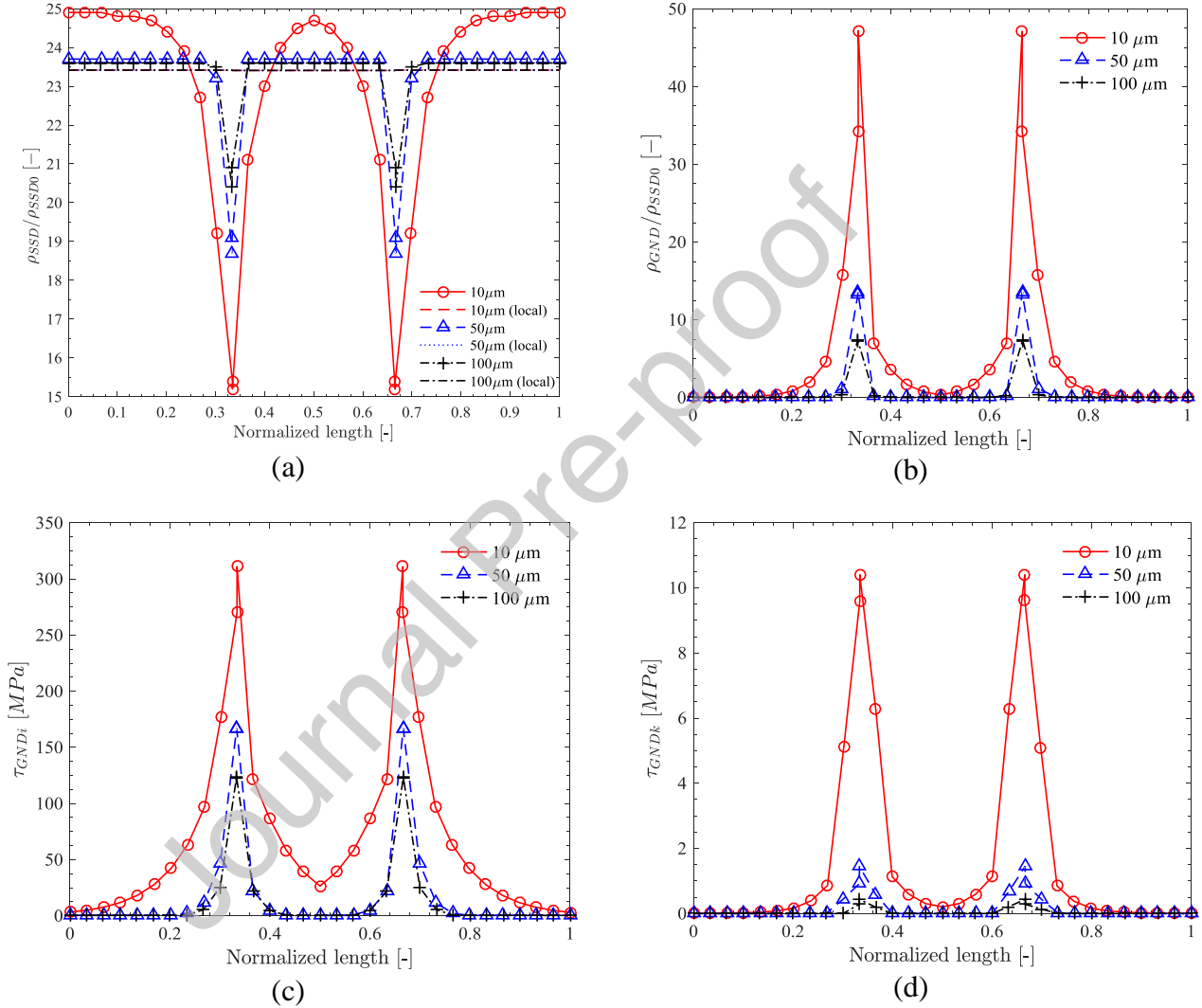
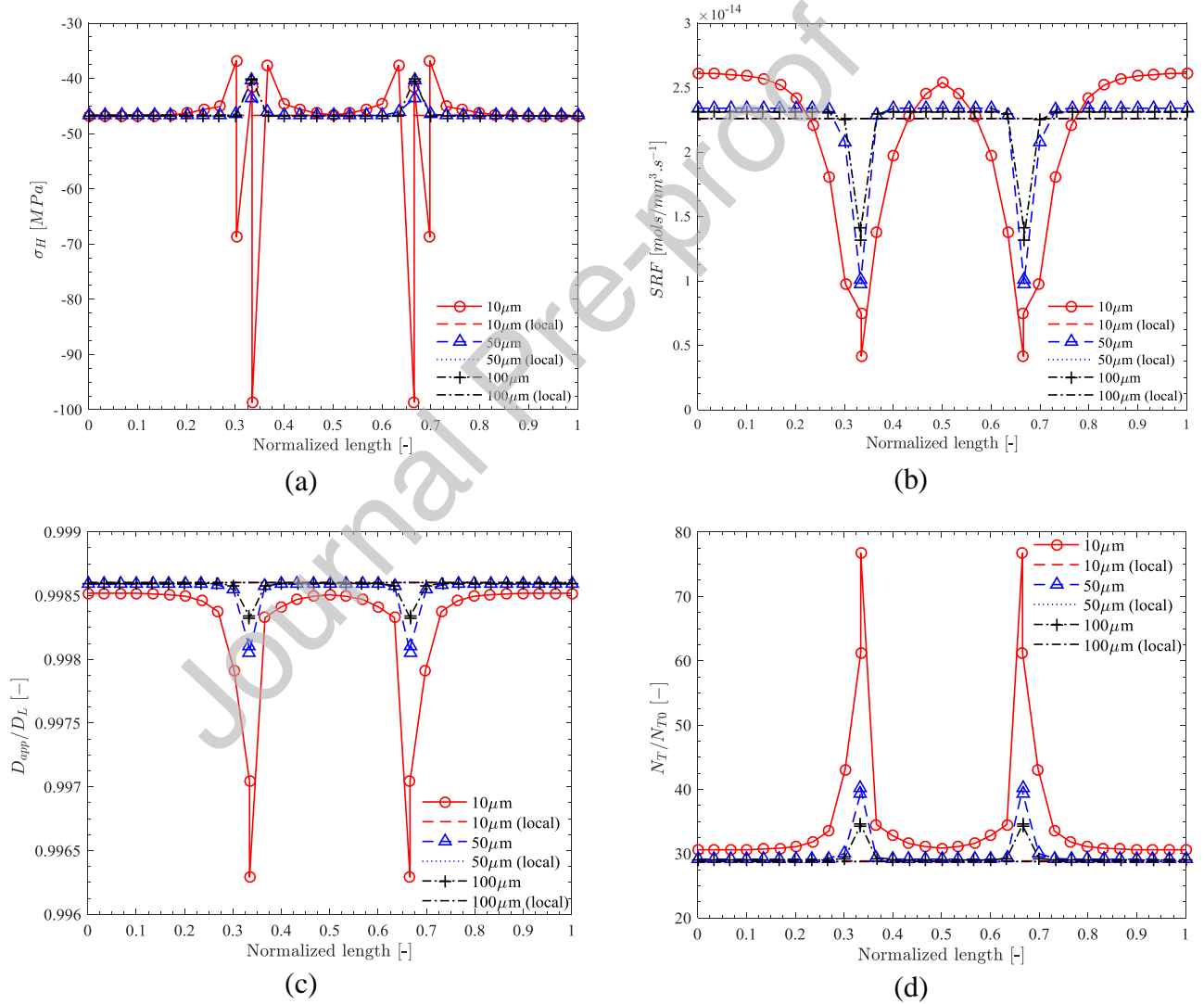


Figure 2: The distribution of (a) normalized SSDs ($\rho_{SSD}/\rho_{SSD0} = \sum_{\alpha=1}^N \rho_{SSD}^{\alpha} / \rho_{SSD0}$), and (b) normalized GNDs ($\rho_{GND}/\rho_{SSD0} = \sum_{\alpha=1}^N \rho_{GND}^{\alpha} / \rho_{SSD0}$) with respect to grain size and correspondingly the evolution of (c) isotropic hardening due to GNDs ($\tau_{GNDi} = \sum_{\alpha=1}^N |\tau_{GNDi}^{\alpha}|$), and (d) back stress due to the pileup of GNDs ($\tau_{GNDk} = \sum_{\alpha=1}^N |\tau_{GNDk}^{\alpha}|$) in the intra- and inter-granular region of the polycrystal specimens after shear deformation along x -direction up to $\gamma_{yx} = 0.33$.

As discussed earlier, the total hydrogen concentration (C_{Tot}) in the microstructure at a material point is the sum of C_L and C_T where $C_T = \sum_{\alpha} C_T^{\alpha}$. The factors that affect the evolution of C_L in the microstructure with deformation are the gradient of lattice hydrogen (∇C_L), gradient of hydrostatic pressure ($\nabla \sigma_H$) and the evolution of trapped hydrogen, C_T . The dependence of C_L on C_T is twofold, first, it reduces the apparent diffusivity, D_{app} , and second, the rate of evolution of C_T affects the

rate of C_L evolution through SRF. The evolution of C_T at a material point with deformation is dependent on the available C_L , N_T ($N_T = \sum_{\alpha} N_T^{\alpha}$) and W_B (see eq. (29)). The role of these factors on the evolution of C_{Tot} is now analysed with respect to variation in grain size of polycrystals.

Due to the strengthening of the inter-granular region by GNDs, this region shows a sharp transition in σ_H as well as SRF compared to the intra-granular region. Grain-size dependent evolution of σ_H and SRF for three polycrystals is shown in Fig. 3(a) and Fig. 3(b), respectively. The increased dislocation density in the inter-granular region also leads to a sharp rise in the trap sites, thus affecting the total hydrogen concentration (C_{Tot}). As only dislocation traps are considered in these simulations, therefore, the effect of W_B vanishes and C_T becomes a function of N_T^{α} and C_L . The variations in the values of D_{app}/D_L and N_T/N_{T0} (wherein $N_{T0} = \frac{\sqrt{3}}{a} \rho_{SSD0}$) in the intra- and inter-granular regions of polycrystals are shown in Fig. 3(c) and Fig. 3(d) respectively, and their corresponding effect on variation in C_L/C_{Tot0} and C_T/C_{Tot0} is shown in Fig. 3(e) and Fig. 3(f), respectively. C_{Tot0} at a material point in the microstructure is the sum of C_{L0} and C_{T0} , where C_{T0} is calculated using N_{T0} in eq. (29).



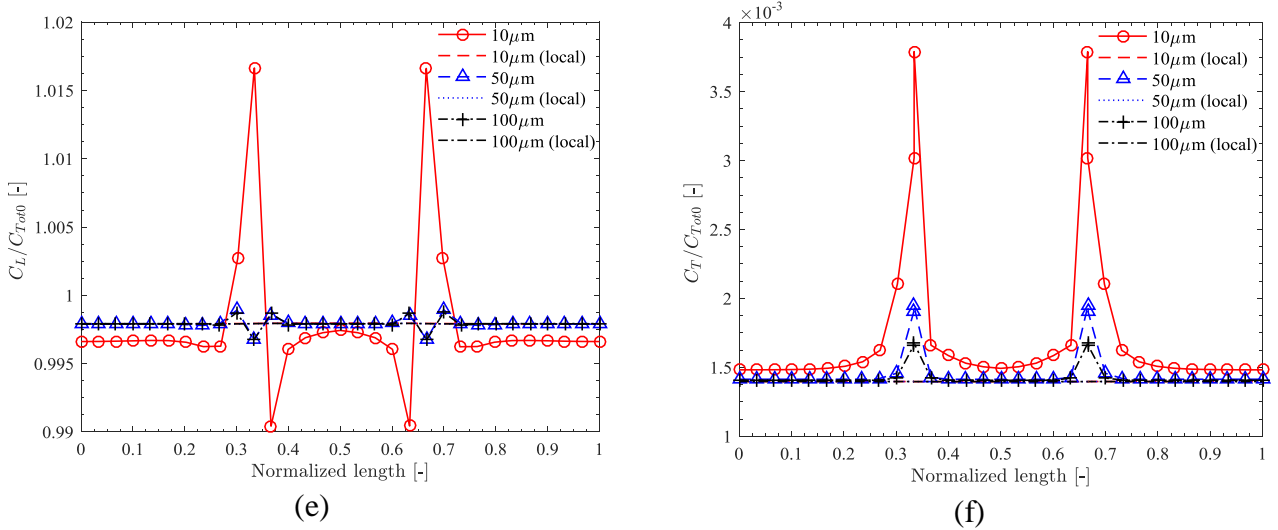


Figure 3: The distribution of (a) hydrostatic pressure (σ_H), (b) slip-rate factor (SRF), (c) normalized apparent diffusivity (D_{app}/D_L), (d) normalized trapping sites (N_T/N_{T0}), (e) normalized hydrogen concentration at NILS (C_L/C_{Tot0}) and (f) normalized hydrogen concentration at trap sites (C_T/C_{Tot0}) at the intra- and inter-granular region of the polycrystal specimens after shear deformation along x -direction up to $\gamma_{yx} = 0.33$. For comparison, the evolution of these quantities using local crystal plasticity model is also shown in all figures.

GNDs at the inter-granular region (or at GB) led to increased N_T compared to the intra-granular (IG) regions, as shown in the plot of N_T versus accumulated plastic slip ($\gamma_{slip}^{acc} = \int_0^T (\sqrt{2/3} \mathbf{L}^p \mathbf{L}^p) dt$), where T is total time of analysis, in Fig. 4(a). While the intra-granular region does not show variation in N_T evolution with deformation for different grain size polycrystals, the evolution of N_T at GB shows a significant difference with grain size. The distribution of C_{Tot} in the polycrystals is thus dependent on several factors and essentially shows a jump at the inter-granular regions irrespective of the grain-size, as shown in Fig. 4(b).

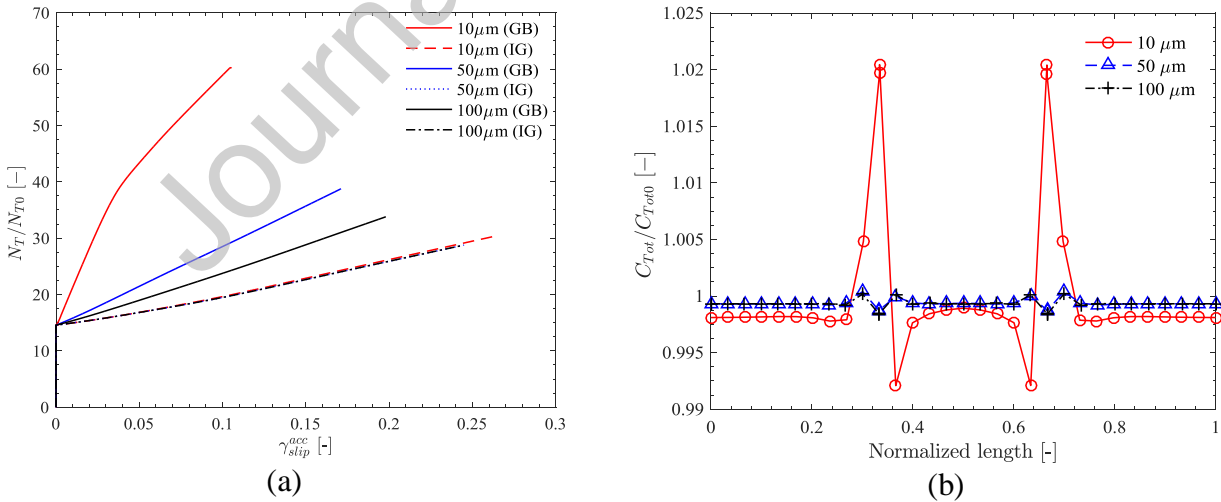


Figure 4: The effect of grain-size on (a) variation of normalized trap density (N_T/N_{T0}) versus accumulated plastic slip (γ_{slip}^{acc}) at the intra-granular (IG) region (calculated at the centre of the middle grain) and grain boundary (GB), and (b) distribution of normalized total hydrogen concentration (C_{Tot}/C_{Tot0}) in different grain-size polycrystal specimens after shear deformation along x -direction up to $\gamma_{yx} = 0.33$.

Out of several factors, the negative value of σ_H (associated with tension) emerges out to be the contributing factor affecting the evolution of C_L in the intra- and inter-granular regions of the polycrystal. C_T , though, clearly followed the trend shown by N_T , the magnitude of C_T is negligible compared to C_L . Thus, the contribution of C_T to C_{Tot} is negligible for the system where only dislocations are considered as trap sites. Such a scenario will change once GBs are also considered as trap sites as will be shown in section 3.4.

For completeness, the coupled framework of non-local CP model and slip-rate based hydrogen transport model is compared with the one that has local CP model to elucidate the role of non-locality on the prediction of hydrogen accumulation in the intra- and inter-granular regions of the polycrystals. Since the local CP model does not include the first and second gradient of \mathbf{F}^P , the evaluation of ρ_{GND} , τ_{GNDi} and τ_{GNDk} at material points cannot be calculated. The variation of ρ_{SSD} in the intra- and inter-granular regions of the polycrystal, as per eq. (7), is only dependent on the misorientation and plastic strain incompatibilities from one grain to another. Due to absence of contribution from GNDs, it leads to a negligible difference in the intra- and inter-granular regions of the polycrystals as shown in the distribution plots of quantities related to deformation (ρ_{SSD}) and hydrogen diffusion (σ_H , SRF , D_{app} , N_T , C_L and C_T) in Fig. 2(a) and Fig. 3 respectively. The jumps in these quantities at GBs (not visible in the figures shown) are due to the orientation difference between the neighbouring grains and show no size effect with the variation in the grain-size. Coupled framework with non-local CP model, on the other hand, clearly differentiates between the intra- and inter-granular regions with respect to variation in ρ_{SSD} and ρ_{GND} that leads to better prediction of hydrogen distribution in the polycrystal specimens with deformation.

3.2 Effect of loading direction on hydrogen distribution in polycrystals

Dislocation density is considered as a primary state variable in the present modelling framework that controls the hardening evolution within the intra- and inter-granular regions of polycrystals. The evolution of dislocation density within grains depends on the number of activated slip systems with deformation which in turn are dependent on the loading direction with respect to the grain boundary plane. Thus, direction of deformation is an important factor controlling the hydrogen distribution within intra- and inter-granular regions of the polycrystals. The loading direction effect is studied by deforming a 10 μm grain size polycrystal along the three mutually perpendicular axes x -, y - and z with respect to the GB plane (see Fig. 1). While deformation along x - and z - directions causes shear, y -direction deformation causes tension in the simulated polycrystals. For shear deformation case, specimens are deformed up to a shear strain $\gamma_{yx} = \gamma_{yz} = 0.33$, and for the tensile loading case, specimens are deformed up to tensile strain, $\epsilon_{yy} = 0.166$ by applying the displacements at the top and bottom surface nodes of the specimen. The strain rate for all the loading cases is fixed at $3.3 \times 10^{-4} \text{ s}^{-1}$, and all the results shown here are at the end of the deformation.

The distribution of ρ_{SSD} and ρ_{GND} in the intra- and inter-granular region of polycrystals deformed along various directions with respect to the GB plane is shown in Fig. 5(a) and Fig. 5(b), respectively. For the tensile loading case, high ρ_{SSD} is observed at the intra-granular regions compared to shear loading cases which is due to the activation of more slip systems. Under tensile and shear loading along x -direction, deformation in intra-granular region is uniform in all three grains whereas during shear loading in the z -direction, the middle grains show less deformation compared to the other two. The inter-granular regions for all loading cases show accumulation of ρ_{GND} . Tensile deformation showed the highest accumulation of ρ_{GND} in the inter-granular regions of the polycrystal. The evolution of ρ_{GND} directly correspond to the strengthening/hardening in terms of τ_{GNDi} , whereas its gradient generates a back-stress (τ_{GNDk}) in the material. The corresponding evolution of τ_{GNDi} and τ_{GNDk} in polycrystal for different loading cases is shown in Fig. 5(c) and Fig. 5(d), respectively. A clear difference in the evolution of non-local terms in the polycrystal with loading direction is observed for the three cases studied.

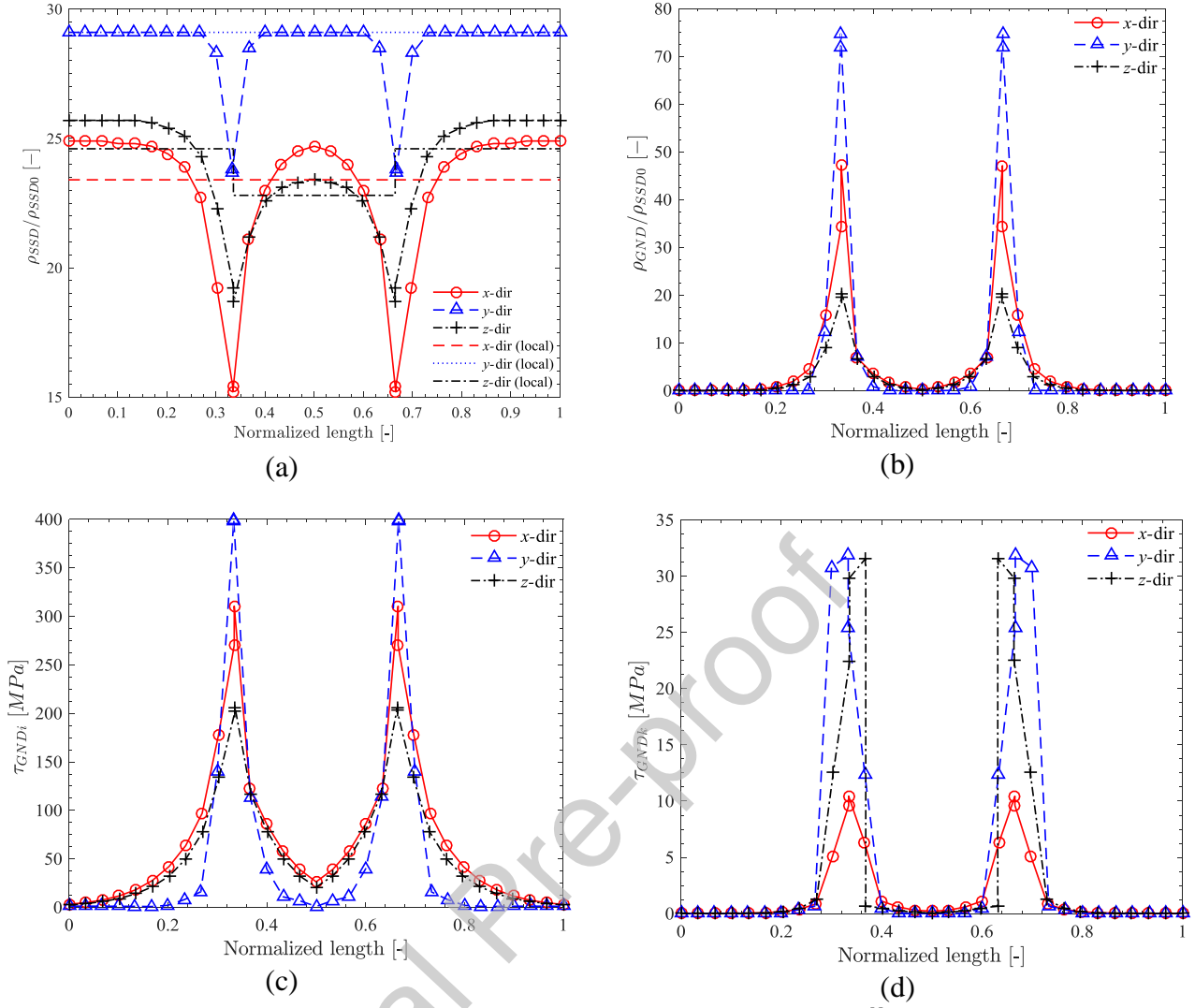
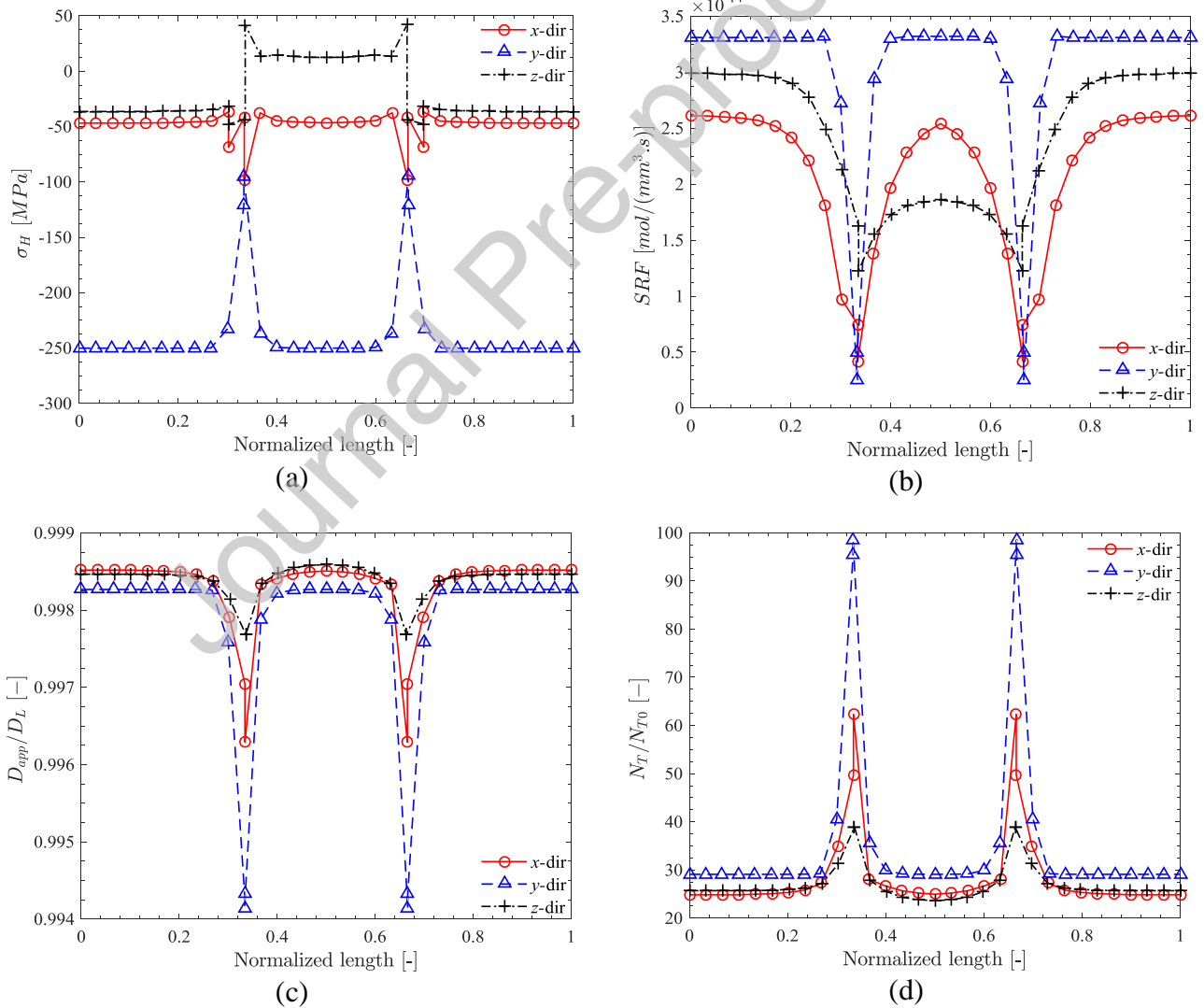


Figure 5: The distribution of (a) normalized SSDs ($\rho_{SSD}/\rho_{SSD0} = \sum_{\alpha=1}^N \rho_{SSD}^{\alpha} / \rho_{SSD0}$), and (b) normalized GNDs ($\rho_{GND}/\rho_{SSD0} = \sum_{\alpha=1}^N \rho_{GND}^{\alpha} / \rho_{SSD0}$) (c) isotropic hardening due to GNDs ($\tau_{GNDi} = \sum_{\alpha=1}^N |\tau_{GNDi}^{\alpha}|$), and (d) back stress due to the pileup of GNDs ($\tau_{GNDk} = \sum_{\alpha=1}^N |\tau_{GNDk}^{\alpha}|$) at the end of deformation along different directions with respect to the GB plane in 10 μm grain size polycrystals.

The effect of loading direction on the distribution of quantities related to hydrogen diffusion in the polycrystal is shown in Fig. 6(a)-(f). Tensile loading (along y -direction) causes highly negative σ_H (associated with tension) in the intra-granular region compared to the inter-granular region that shows a less negative σ_H (associated with reduced tension). Shear loading along both x - & z -directions causes sharp jumps in σ_H at the GBs, see Fig. 6(a). The gradient of σ_H affects the chemical potential of hydrogen and attracts more C_L to the regions where it is less, see eq. (20). Among various factors, the local slip-rate factor also affects C_L evolution in the microstructure. For all loading cases, the evolution of strong τ_{GNDi} at the inter-granular region (Fig. 5(c)) made this region stronger compared to intra-granular region. This led to increased material flow in the intra-granular region to accommodate the imposed deformation. Thus, the slip-rate factor in the polycrystal is suppressed at the inter-granular region and enhanced at intra-granular regions. For shear deformation case along the z -direction, the loading direction is parallel to one of the slip systems in top and bottom grains enhancing the magnitude of slip-rate factor in these grains compared to middle grain. This causes top and bottom grains to deform more compared to the middle one, and lesser difficulty to plastic flow generates fewer GNDs, as can be seen in Fig. 5(a) and Fig. 5(b). This further develops less N_T at intra-granular regions and consequently higher D_{app}

can be seen in Fig. 6(d) and Fig. 6(c), respectively. The evolution of D_{app} is shown in Fig. 6(c) with low values at the inter-granular region compared to the intra-granular region due to enhanced N_T at the inter-granular region, as shown in Fig. 6(d). For the insulated system studied here, the distribution of C_L in the polycrystal is directly proportional to the negative σ_H distribution, D_{app} and inversely proportional to slip-rate factor. Thus, C_L distribution in the polycrystal depends on the competition between the effects of σ_H , D_{app} and SRF. The combined effect of these three quantities on the distribution of C_L for all loading cases is shown in Fig. 6(e). The distribution of C_T in polycrystal (as shown in Fig. 6(f)) with loading along x -, y - and z - directions is dependent on quantities such as C_L and N_T at a material point with deformation.

The plot of N_T versus accumulated plastic slip particularly at intra-granular region and GB is shown in Fig. 7(a). The GB region under all types of loadings showed the highest evolution of N_T compared to the intra-granular region. The GBs in the tensile loading case emerged-out with highest N_T as well as accumulated plastic slip due to the strong evolution of GNDs. The distribution of C_{Tot} as a sum of C_L and C_T affected by the change in loading direction along the polycrystal is shown in Fig. 7(b). Shear loading cases accumulated more hydrogen at GBs compared to the tensile loading case, primarily due to low chemical potential caused by negative gradient of σ_H at the GBs (see eq. (20)) and controlled evolutions of GNDs compared to tensile loading case.



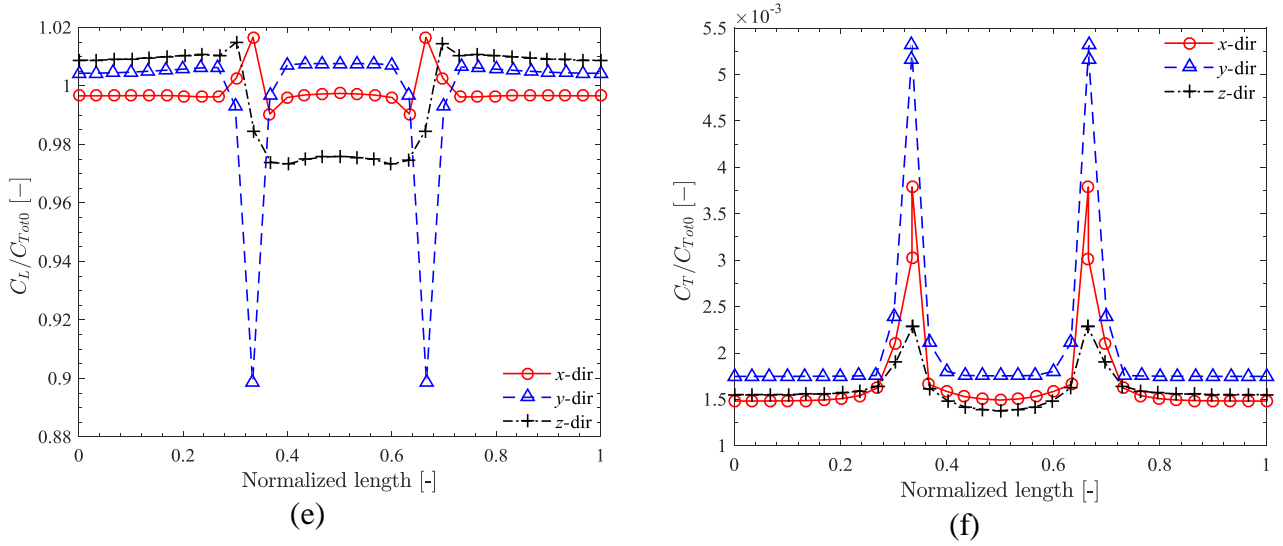


Figure 6: The effect of loading direction with respect to GB plane on (a) the distribution of σ_H , (b) slip-rate factor (SRF), (c) normalized apparent diffusivity (D_{app}/D_L), (d) normalized trapping sites (N_T/N_{T0}), (e) normalized hydrogen concentration at NILS (C_L/C_{Tot0}), and (f) normalized hydrogen concentration at trap sites (C_T/C_{Tot0}) in 10 μm grain size polycrystal after deformation.

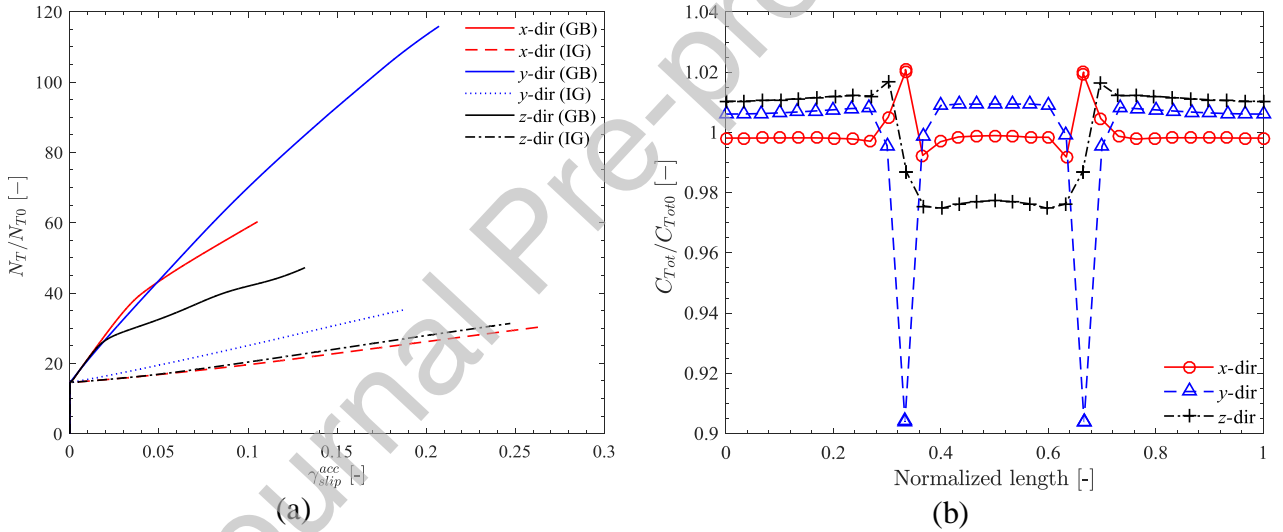


Figure 7: The effect of loading direction with respect to the GB plane on (a) variation of normalized trap density (N_T/N_{T0}) versus accumulated plastic slip (γ_{slip}^{acc}) at the intra-granular (IG) region (calculated at the centre of the middle grain) and grain boundary (GB) of the simulated polycrystals, and (b) the distribution of total hydrogen concentration (C_{Tot}/C_{Tot0}) with respect to the normalized length of the polycrystal.

3.3 Effect of strain-rate on hydrogen distribution in polycrystals

Given that the hydrogen transport within metals is a transient process, hydrogen embrittlement is thus very sensitive to strain rates under both monotonic as well as cyclic loading cases (Krom et al., 1999; Momotani et al., 2017). The coupled framework includes the effect of strain-rate on hydrogen evolution in the polycrystal during deformation through the SRF (see (32)). In this section, first, the effect on SRF on C_L evolution in various grain size polycrystals is identified by performing simulations with and without the SRF included in the modelling framework. Second, the role of strain-rate on total hydrogen distribution in the 10 μm grain size polycrystal deformed under shear along x -direction upto $\gamma_{yx} = 0.33$ at a constant strain-rate $3.3 \times 10^{-4} \text{ s}^{-1}$ is analysed.

In the coupled framework, the SRF is introduced to provide the correct balance between lattice and trap hydrogen at a material point in the polycrystal (Krom et al., 1999). The effect of SRF on C_L distribution in various grain size polycrystals after the deformation is shown in Fig. 8. In bigger grains (50 and 100 μm) polycrystals, the SRF has uniformly reduced the C_L value throughout the polycrystal. In the smallest grain polycrystal, the SRF also decreased the C_L in the polycrystal, but only in the intra-granular regions. This is attributed to the strengthened inter-granular regions due to the evolution of non-local terms there that led to the negligible contribution of SRF to C_L evolution in the inter-granular regions. It shows that the SRF is able to incorporate the effects of local slip rates on the evolution of total hydrogen.

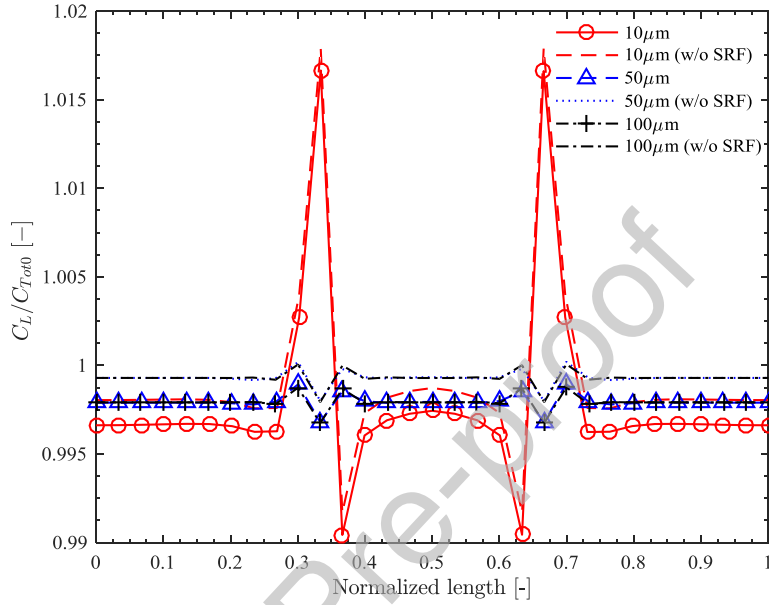


Figure 8: Effect of slip-rate factor (SRF) on the evolution of normalized lattice hydrogen concentration (C_L/C_{Tot0}) in various grain-size polycrystals. Result of two sets of simulations are shown, one with SRF and one without SRF included in hydrogen transport model (eq. (32)) to highlight its role on C_L evolution in the polycrystal.

To analyse the role of strain-rates on hydrogen distribution in microstructure, strain-rates ranging from $3.3 \times 10^{-5} \text{ s}^{-1}$ to $3.3 \times 10^{-2} \text{ s}^{-1}$ are applied during shear deformation along x -direction on a 10 μm grain size polycrystal. The nickel polycrystals with 10 μm grain-size at room temperature, however, are reported to be strain-rate insensitive (Schwaiger et al., 2003). This is incorporated in the modelling framework by choosing the low value of exponent, $n = 20$ in the flow rule given in eq. (17). The ineffectiveness of strain-rate to change the dislocation configuration is also shown by our results in Fig. 9(a) where the evolution of N_T with respect to accumulated plastic slip at various strain-rates is same for both intra-granular regions as well as at GBs. The modelling of the strain-rate effect is facilitated by SRF evolution in the polycrystal, as shown in Fig. 9(b). In the coupled framework, the increased magnitude of SRF at high strain-rates compensates for the reduction in C_L . The corresponding reduction in C_L then further reduces C_T (using the considered equilibrium between their respective occupancies) as well as C_{Tot} distribution throughout the polycrystals, as shown in Fig. 9(c).

Fig. 9(d) shows the effect of strain rate on total hydrogen concentration at GBs which are the sites of maximum hydrogen concentration in the insulated polycrystals. A plateau is reached in the maximum hydrogen concentration with decreasing strain rate. This suggests that slow strain-rate deformations are more prone to hydrogen embrittlement compared to high strain rate deformations, which is also observed experimentally for both monotonic and fatigue loading cases (Doshida and

Takai, 2014; Momotani et al., 2017; Murakami and Matsuoka, 2010). A strain rate of the order of 10^{-3} s^{-1} appears to be critical above which the hydrogen accumulation at the inter-granular regions starts decreasing from the initial concentration.

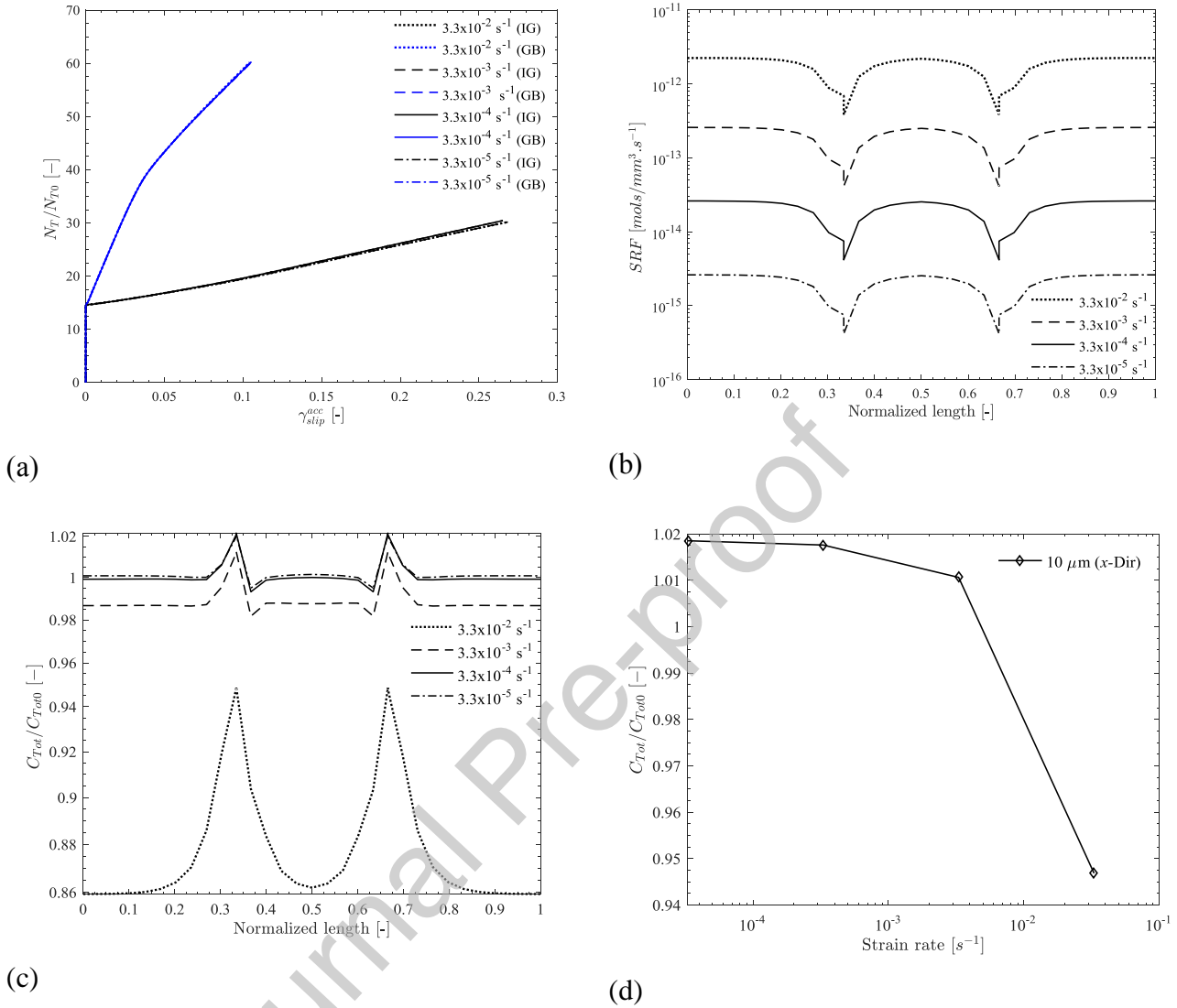


Figure 9: The effect of strain rate on (a) variation of normalized trap density (N_T/N_{T0}) versus accumulated plastic slip (γ_{slip}^{acc}) at the intra-granular (IG) region (calculated at the centre of the middle grain) and grain boundary (GB) of the simulated polycrystals, and (b) the distribution of slip-rate factor (SRF), (c) normalized total hydrogen concentration (C_{Tot}/C_{Tot0}) throughout the polycrystals, and (d) at GB of a $10 \mu\text{m}$ grain-size polycrystal.

3.4 Role of GB character on hydrogen distribution in polycrystals

A metallic polycrystal consists not only of dislocation traps for hydrogen but also various other traps like vacancies, phase/grain boundaries that have different binding energies and can affect the hydrogen diffusivity differently. For a single phase metallic polycrystals, GB traps play a significant role in hydrogen distribution with deformation depending on the crystallographic character of GBs (where the character of the GB is defined by their atomic arrangement) (Bechtle et al., 2009). It is reported that the high angle special GBs (characterised by a particular misorientation of adjoining grains leading to high degree of atomic matching and low excess free volume) have different hydrogen diffusivity and binding energy compared to the intra-granular regions which primarily consists of only dislocation traps (Di Stefano et al., 2015; Oudriss et al., 2012b, 2012a).

In this section, the effect of grain boundary diffusivity and binding energy is investigated on the hydrogen distribution in the polycrystals with deformation. Two different types of special GBs i.e., $\Sigma 3$ and $\Sigma 5$ are considered in this study, in which the former is a representative of a perfect GB in fcc crystals having the lowest GB energy and latter is a representative of a general GB having a more open structure and high GB energy. The choice of these two GB type is made such that one of the GB type (i.e. $\Sigma 3$) has higher binding energy compared to dislocations ($W_B^{\Sigma 3} > W_B^{\text{dis}}$) to represent a weak GB trap and other (i.e. $\Sigma 5$) has lower binding energy than dislocations ($W_B^{\Sigma 5} < W_B^{\text{dis}}$) to represent a strong GB trap. In addition, $\Sigma 3$ GB has lower diffusivity and $\Sigma 5$ GB has higher diffusivity of hydrogen compared to the intra-granular region. The values of these parameters are calculated using density functional theory by Di Stefano et al. (2015), refer Table 2. Therefore, $\Sigma 5$ GB will act as a two-dimensional sink for hydrogen compared to $\Sigma 3$ GB which will act as a two-dimensional barrier for hydrogen distribution in the polycrystal with deformation.

To understand the role of the crystallographic character of special GBs, 10 μm grain size polycrystals consisting of both GBs as $\Sigma 3$ and $\Sigma 5$ GBs are deformed under shear along the x -direction (upto $\gamma_{yx} = 0.33$). Elements adjacent to GBs in the top and bottom grains are considered as GB elements (GBEs) by assigning them the diffusivity and binding energy values mentioned in Table 2. The GBE thickness though is about two order higher than the GB thickness in realistic polycrystals, the simplified model used here is helpful to understand the mechanistic role of GB type on hydrogen distribution in the polycrystal with deformation. Consequently, the effect of GB type on the distribution of both deformation and hydrogen-related quantities are shown in Fig. 10.

For the $\Sigma 3$ GBs containing polycrystal, similar deformation is observed at the intra-granular regions of all three grains compared to $\Sigma 5$ GBs containing polycrystal where the maximum deformation is observed in the middle grain, as shown by the distribution of ρ_{SSD} in the polycrystal in Fig. 10(a). This is due to favorable orientation of the middle grain to the applied shear deformation, generating increased stretch and SSDs in the $\Sigma 5$ GBs containing polycrystal. The $\Sigma 3$ GBs containing polycrystal, however, showed increased hardening in the inter-granular region compared to the $\Sigma 5$ GBs containing polycrystal, as shown by the evolution of ρ_{GND} in Fig. 10 (b). The $\Sigma 5$ GBs containing polycrystal also showed a plateau of constant ρ_{GND} in the inter-granular region of the middle grain (a softer grain) due to localized bending caused by imposed shear deformation. The negative pressure value (associated with tension), as shown in Fig. 10(c), throughout the $\Sigma 3$ GBs containing polycrystal confirms the overall stretching of all three grains. However, stretching is observed only in the middle grain of the $\Sigma 5$ GBs containing polycrystal while both top and bottom grains are under compression (positive pressure value associated with compression). This leads to severe jump in the σ_H value at the inter-granular region of $\Sigma 5$ GBs containing polycrystal compared to the $\Sigma 3$ GBs containing polycrystal.

The distribution of lattice hydrogen concentration (C_L) in the $\Sigma 3$ and $\Sigma 5$ GBs containing polycrystals, as shown in Fig. 10(d), is in direct correspondence with σ_H distribution in these polycrystals. High diffusivity and strong trapping effect of $\Sigma 5$ type GBEs in the top and bottom grains of the polycrystal decreased the lattice hydrogen concentration throughout the polycrystal while sharply increasing the trap hydrogen concentration (C_T) in the GBEs, as shown in Fig. 10(e). This scenario is not observed in the $\Sigma 3$ GBs containing polycrystal due to the low value of diffusivity and weak binding effect associated with $\Sigma 3$ type GBEs in the top and bottom grains. Due to the competition between the effect of trap binding energy and σ_H value on hydrogen distribution within the polycrystal, two separate peaks can be seen in the total hydrogen concentration (C_{Tot}) for $\Sigma 5$ GBs containing polycrystal in Fig. 10 (f) which is not there for the case of $\Sigma 3$ GBs containing polycrystal.

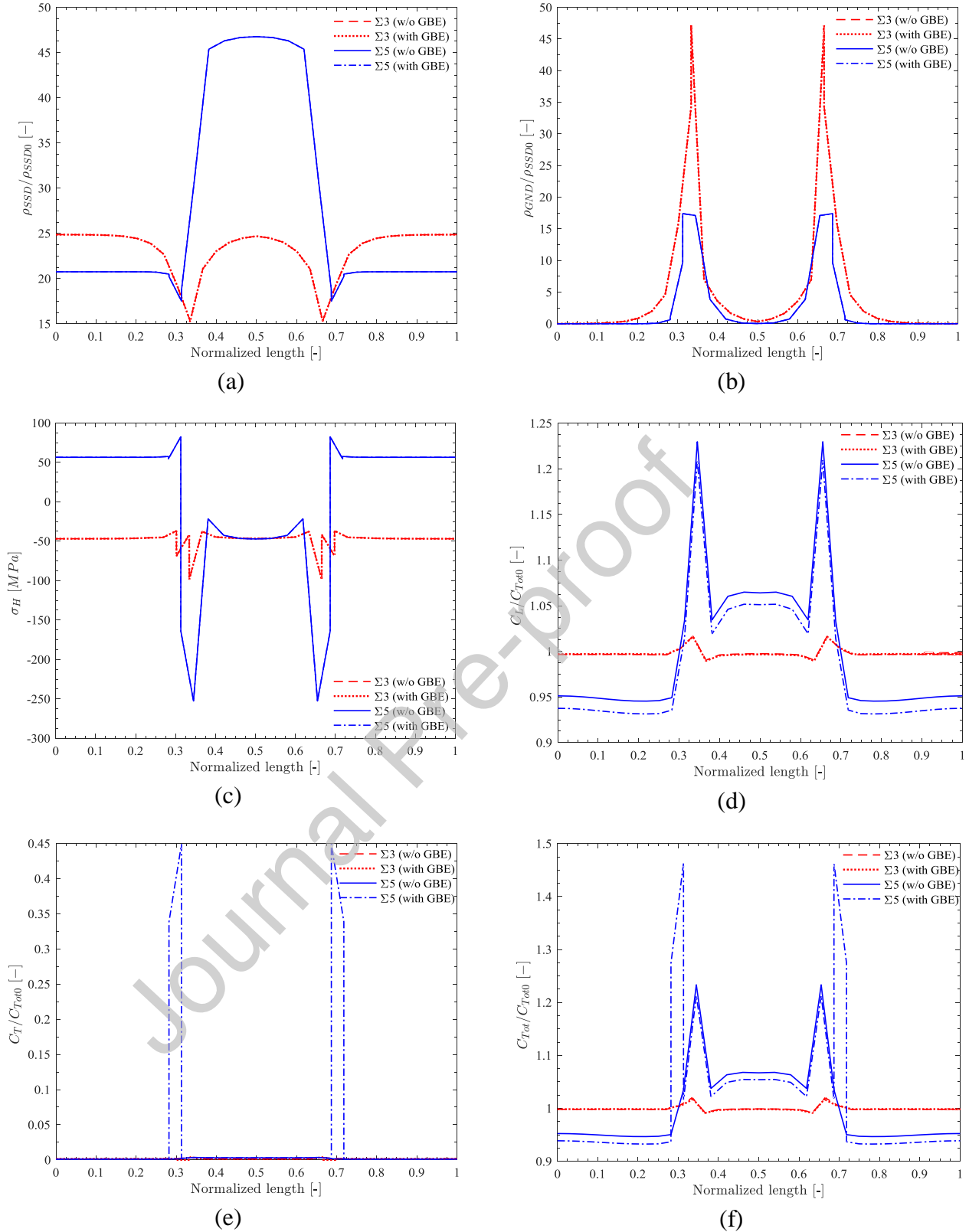


Figure 10: The distribution of both deformation and hydrogen diffusion related quantities in the $\Sigma 3$ and $\Sigma 5$ GBs containing polycrystal after shear deformation along x-direction. (a) Normalized SSDs ($\rho_{SSD}/\rho_{SSD0} = \sum_{\alpha=1}^N \rho_{SSD}^{\alpha}/\rho_{SSD0}$), (b) normalized GNDs ($\rho_{GND}/\rho_{SSD0} = \sum_{\alpha=1}^N \rho_{GND}^{\alpha}/\rho_{SSD0}$), (c) hydrostatic pressure (σ_H), (d) normalized hydrogen concentration at NILS (C_L/C_{Tot0}), (e) normalized hydrogen concentration at trap sites (C_T/C_{Tot0}), and (f) total hydrogen concentration (C_{Tot}/C_{Tot0}) distribution along the length of polycrystal.

4 Discussion

Estimating accurate hydrogen distribution in the metallic microstructure with deformation provides an opportunity to understand the underlying mechanisms associated with the hydrogen embrittlement phenomenon. Enhanced hydrogen segregation in the microstructure plays a key role in the embrittlement as it controls the crack initiation in the microstructure. To better understand the role of microstructure on hydrogen segregation, a coupled framework of non-local dislocation density-based crystal plasticity model and slip-based hydrogen transport model is developed to study the hydrogen distribution in a simplified polycrystal model with deformation. The novel framework accurately captured the effect of microstructural features such as grain size and crystallographic character of GBs in the polycrystal as well as external factors such as loading direction and strain-rate on hydrogen distribution within the microstructure with deformation.

The role of grain size on hydrogen distribution and segregation with deformation is shown using 10, 50 and 100 μm average grain size polycrystal specimens. The evolution of ρ_{SSD} and ρ_{GND} that constitute the total dislocation density is affected by average grain-size in the polycrystal. Fine-grained polycrystals show more evolution of GNDs with deformation at the inter-granular regions compared to coarse grained polycrystals. Eventually, significant τ_{GNDi} emerged out in the fine-grained polycrystal leading to the strengthening of the inter-granular regions, whereas the evolution of τ_{GNDk} led to the evolution of back stress. The evolution of these non-local terms at the inter-granular regions caused enhanced deformation in the GND free intra-granular region of fine-grained polycrystal to accommodate the applied deformation. These observations associated with the evolution of non-local terms on the strengthening of microstructure are consistent with Ma and Hartmaier (2014). The evolution of non-local terms due to smaller grain size affected the distribution of quantities related to the hydrogen diffusion such as $\nabla\sigma_H$, D_{app} , SRF and N_T that in turn control the distribution of C_{Tot} in the polycrystal through C_L and C_T . These results are consistent with the experiments where high hydrogen concentration is found in fine-grained samples in comparison with coarse-grained samples (Chen et al., 2014; Park et al., 2017). However, despite of accumulating high hydrogen concentration at GBs, fine-grained samples are reported to show superior resistance to HE. This is due to high GB area per unit volume in fine-grained materials giving rise to less normalized hydrogen concentration compared to coarse-grained polycrystals that were electrochemically charged with the same internal hydrogen concentration (Park et al., 2017; Zan et al., 2015). In correlation with these experimental results, the dependence of grain-size on activation of a particular hydrogen embrittlement mechanism is provided by Zan et al. (2015) where they suggested the association of HELP mechanism with fine-grained sample and HEDE with coarse-grain sample.

The difference in loading direction with respect to the GB plane affects the evolution of ρ_{SSD} and ρ_{GND} in the intra- and inter-granular regions of the polycrystals. Tensile loading led to the increased evolution of ρ_{SSD} and ρ_{GND} compared to shear loading case in the intra- and inter-granular regions respectively. These results are consistent with the experimental study where a strong dependence of loading direction on the dislocation evolution at the vicinity of twin boundaries is shown (Jun et al., 2018; Lu et al., 2017). They observed that when the loading direction is perpendicular to twin boundary, more dislocations emerged compared to the case when loading direction is parallel to twin boundary. Furthermore, the increased ρ_{GND} at the inter-granular regions led to sharp stress jump for the tensile loading case causing positive σ_H compared to shear loading case. The total hydrogen concentration is, therefore, found to be less in inter-granular regions for tensile loading case compared to shear loading case in x - and z - directions. These results show that for fine-grain polycrystal, shear deformations can be more damaging to cause inter-granular failure compared to tensile deformation depending on the orientation of neighbouring grains. Such a claim however needs to be validated through small scale experiments that currently is not available in literature and are being performed in our group.

Despite of the pronounced dislocation density evolved after significant plastic deformation, as shown in figures 4(a) and 7(a), the values of C_T remained two orders less compared to C_L . This is attributed to low binding energy of dislocations in fcc metals leading to the easy release of hydrogen from dislocations into the metal lattice. Due to this, negligible change is observed in D_{app} as shown in Fig. 3(c) and 6(c).

Another factor that affected the hydrogen distribution in the microstructure is the strain-rate used for deformation. Total hydrogen concentration is found to decrease at GBs when strain-rate is increased. Since only saturable and reversible traps such as dislocations are considered for these simulations, the reduction in the occupancy of lattice hydrogen at high strain-rate attracts hydrogen from traps sites leading to the reduction in occupancy in trap sites. Eventually, total hydrogen concentration is reduced at high strain-rates which is incorporated in the coupled framework through slip-rate factor. The plastic flow evolution in polycrystalline nickel with grain-size of 1 μm and more is observed to be strain-rate insensitive at room temperature and considered strain-rate in this work (Schwaiger et al., 2003). Moreover, at high strain-rates, the dislocation velocity increases to accommodate rapid deformation where dislocation density remains almost unaffected (Gilbert et al., 1965). As also suggested by Krom et al. (1999), at higher dislocation velocity than the diffusivity of hydrogen, fast-moving dislocations become hydrogen-free, thus removing the assistance given by hydrogen for dislocation motion under HELP mechanism (Krom et al., 1999). Whereas at lower strain-rates, hydrogen atoms remain trapped at the core of dislocation causing continuous damage to the material by invoking HELP mechanism (Barnoush and Vehoff, 2008). This leads to the reduced effect of hydrogen on the deformation of the material due to reduced susceptibility to HE at high strain rates. Our results show high hydrogen concentration at GBs when strain-rate is lower than the critical strain rate, i.e. $< 10^{-3} \text{ s}^{-1}$. The effect of strain-rate on hydrogen evolution is in accordance with the results in literature, where the critical strain rate for nickel is $10^{-4} - 10^{-3} \text{ s}^{-1}$ (Bal et al., 2016), and provide the validation of the coupled modelling framework. In all simulations discussed above, the distribution of total hydrogen within the polycrystal is mainly governed by C_L while C_T contribution is negligible. This is due to the consideration of dislocations only traps in the microstructure that has a low value of trap binding energy in the above-discussed simulations.

In fcc metals, GBs are other types of traps available in the single phase polycrystals that are reported to control the hydrogen distribution within the microstructure depending on their crystallographic character. The interaction of hydrogen with GBs is defined by their binding energy, (W_B^{GB}) and average diffusivity, (D_{GB}) at GBs. The role of GB diffusivity and binding energy on hydrogen distribution in a deforming polycrystals is studied for two different polycrystals consisting of $\Sigma 3$ and $\Sigma 5$ type GBs such that $W_B^{\Sigma 3} > W_B^{\text{dis}}$ and $W_B^{\Sigma 5} < W_B^{\text{dis}}$. It is shown that GBs with weaker hydrogen trapping affect compared to dislocation trap (i.e. $\Sigma 3$ GB) doesn't affect the hydrogen distribution, whereas, GBs with stronger hydrogen trapping affect compared to dislocation trap (i.e. $\Sigma 5$ GB) plays a significant role in controlling the hydrogen distribution behaviour in polycrystals. However, the role of trap density on the hydrogen distribution at both types of GBs needs to be identified before a proper understanding can be made. In this regard, GB engineering has become an important tool to mitigate hydrogen embrittlement by controlling the hydrogen segregation and transportation in the metallic microstructure by designing the microstructure with optimum GB types (Bechtle et al., 2009). $\Sigma 3$ GBs are known to be more resistant to inter-granular failure due to their ideal atomic structure that doesn't allow hydrogen segregation compared to $\Sigma 5$ GBs which is in-line with the results obtained in this work.

5 Conclusion

A novel modelling framework is presented to simulate the role of microstructural factors such as grain size, crystallographic character of GB as well as external factors such as loading direction with respect to GB plane and strain rate on hydrogen distribution and segregation in the metallic

microstructure with deformation. The effect of these factors on hydrogen evolution is modelled using a non-local dislocation density-based crystal plasticity model coupled with slip-rate based hydrogen transport model which is capable of incorporating additional hardening through the evolution of GNDs and back stresses caused by their pileup at the inter-granular regions. Hydrogen trapping in dislocations is considered along different slip systems in addition to the GB traps, the effect of which is explicitly included in the inter-granular region using specific trap binding energy and diffusivity. Following conclusions are drawn from the hydrogen distribution and segregation analyses using a simplified virtual metallic polycrystal pre-charged with hydrogen under deformation:

- In the case when microstructure contains only weak hydrogen traps e.g. dislocations in fcc metals, the distribution of hydrogen in the microstructure is mainly dependent on the hydrostatic pressure distribution.
- Grain size affects hydrogen segregation at the inter-granular regions of the microstructure both due to change in dislocation/trap density (through C_T) as well as hydrostatic pressure (through C_L).
- Variation in the loading direction with respect to GB plane leads to variation in the amount of deformation at the intra- and inter-granular regions of neighbouring grains, making them either hard or soft depending on their orientation. Soft grains accommodate more deformation and show high concentration of hydrogen due to increased dislocation density.
- The inter-granular regions between the soft and hard grains are the regions of high hydrogen concentration due to evolution of high local hydrostatic pressure.
- Strain-rate affects the distribution of total hydrogen concentration in the microstructure based on the local slip-rates. Higher slip-rate at a material point leads to decrease in the total hydrogen concentration.
- Grain boundaries as trap sites can significantly affect the hydrogen segregation at GBs and distribution in the microstructure provided their trap binding energies are high compared to dislocation traps.

The present model can be further extended to simulate the hydrogen-based damage in the metallic microstructure under both monotonic as well as cyclic loadings. The effects of hydrogen such as rise in stage 1 hardening due to dislocation pinning, prolonged slip on primary slip systems causing a delay in emergence of stage 2 hardening and high stage-2 hardening due to reduced cross-slip on the deformation behaviour of single crystals, as observed by Delafosse et al. (2008), can be incorporated in future. Traps other than dislocation such as vacancies can also be incorporated in the present framework which stands as an ideal start point for such explorations.

Conflict of Interest

All authors have participated in (a) conception and design, or analysis and interpretation of the data; (b) drafting the article or revising it critically for important intellectual content; and (c) approval of the final version.

This manuscript has not been submitted to, nor is under review at, another journal or other publishing venue.

The authors have no affiliation with any organization with a direct or indirect financial interest in the subject matter discussed in the manuscript

Acknowledgement

The authors wish to extend their sincere thanks to the Science & Engineering Research Board (SERB), Department of Science & Technology, Government of India, for providing support for this work under SR/FTP/ETA-0118/2014.

References

- Angelo, J.E., Moody, N.R., Baskes, M.I., 1995. Trapping of hydrogen to lattice defects in nickel. *Model. Simul. Mater. Sci. Eng.* 289–307. <https://doi.org/https://doi.org/10.1088/0965-0393/3/3/001>
- Bal, B., Koyama, M., Gerstein, G., Maier, H.J., Tsuzaki, K., 2016. Effect of strain rate on hydrogen embrittlement susceptibility of twinning-induced plasticity steel pre-charged with high-pressure hydrogen gas. *Int. J. Hydrogen Energy* 41, 15362–15372. <https://doi.org/10.1016/j.ijhydene.2016.06.259>
- Barnoush, A., Vehoff, H., 2008. In situ electrochemical nanoindentation : A technique for local examination of hydrogen embrittlement. *Corros. Sci.* 50, 259–267. <https://doi.org/10.1016/j.corsci.2007.05.026>
- Barrera, O., Tarleton, E., Tang, H.W., Cocks, A.C.F., 2016. Modelling the coupling between hydrogen diffusion and the mechanical behaviour of metals. *Comput. Mater. Sci.* 122, 219–228. <https://doi.org/10.1016/j.commatsci.2016.05.030>
- Beachem, C.D., 1972. A new model for hydrogen-assisted cracking (hydrogen “embrittlement”). *Metall. Trans.* 3, 441–455. <https://doi.org/https://doi.org/10.1007/BF02642048>
- Bechtle, S., Kumar, M., Somerday, B.P., Launey, M.E., Ritchie, R.O., 2009. Grain-boundary engineering markedly reduces susceptibility to intergranular hydrogen embrittlement in metallic materials. *Acta Mater.* 57, 4148–4157. <https://doi.org/10.1016/j.actamat.2009.05.012>
- Birnbaum, H.K., Sofronis, P., 1994. Hydrogen-enhanced localized plasticity-a mechanism for hydrogen-related fracture. *Mater. Sci. Eng. A* 176, 191–202. [https://doi.org/https://doi.org/10.1016/0921-5093\(94\)90975-X](https://doi.org/https://doi.org/10.1016/0921-5093(94)90975-X)
- Chen, S., Zhao, M., Rong, L., 2014. Effect of grain size on the hydrogen embrittlement sensitivity of a precipitation strengthened Fe – Ni based alloy. *Mater. Sci. Eng. A* 594, 98–102. <https://doi.org/10.1016/j.msea.2013.11.062>
- Dadfarnia, M., Martin, M.L., Nagao, A., Sofronis, P., Robertson, I.M., 2014. Modeling hydrogen transport by dislocations. *J. Mech. Phys. Solids* 78, 511–525. <https://doi.org/10.1016/j.jmps.2015.03.002>
- Delafosse, D., Feaugas, X., Aubert, I., Saintier, N., Olive, J., 2008. Effects of Hydrogen on Materials, in: Somerday, B., Sofronis, P., Jones, R. (Eds.), *Proceedings of the 2008 International Hydrogen Conference*. pp. 78–87.
- Devincre, B., 1995. Three dimensional stress field expressions for straight dislocation segments. *Solid State Commun.* 93, 875–878. [https://doi.org/https://doi.org/10.1016/0038-1098\(94\)00894-9](https://doi.org/https://doi.org/10.1016/0038-1098(94)00894-9)
- Di Stefano, D., Mrovec, M., Elsässer, C., 2015. First-principles investigation of hydrogen trapping and diffusion at grain boundaries in nickel. *Acta Mater.* 98, 306–312. <https://doi.org/10.1016/j.actamat.2015.07.031>
- Djukic, M.B., Bakic, G.M., Zeravcic, V.S., Sedmak, A., 2019. The synergistic action and interplay of hydrogen embrittlement mechanisms in steels and iron : Localized plasticity and

- decohesion. *Eng. Fract. Mech.* 216, 106528.
<https://doi.org/10.1016/j.engfracmech.2019.106528>
- Djukic, M.B., Zeravcic, V.S., Bakic, G.M., Sedmak, A., Rajicic, B., 2015. Hydrogen damage of steels : A case study and hydrogen embrittlement model. *EFA* 58, 485–498.
<https://doi.org/10.1016/j.engfailanal.2015.05.017>
- Doshida, T., Takai, K., 2014. Dependence of hydrogen-induced lattice defects and hydrogen embrittlement of cold-drawn pearlitic steels on hydrogen trap state, temperature, strain rate and hydrogen content. *Acta Mater.* 79, 93–107. <https://doi.org/10.1016/j.actamat.2014.07.008>
- E Orowan, 1940. Problems of plastic gliding. *Proc. Phys. Soc.* 52, 8.
<https://doi.org/https://doi.org/10.1088/0959-5309/52/1/303>
- Engels, P., Ma, A., Hartmaier, A., 2012. Continuum simulation of the evolution of dislocation densities during nanoindentation. *Int. J. Plast.* 38, 159–169.
<https://doi.org/https://doi.org/10.1016/j.ijplas.2012.05.010>
- Feaugas, X., Haddou, H., 2007. Effects of grain size on dislocation organization and internal stresses developed under tensile loading in fcc metals. *Philos. Mag.* 87, 989–1018.
<https://doi.org/10.1080/14786430601019441>
- Fukai, Y., 2003. Superabundant Vacancies Formed in Metal – Hydrogen Alloys. *Phys. Scripta.* T103, 11–14. <https://doi.org/https://doi.org/10.1238/Physica.Topical.103a00011>
- Gilbert, A., Wilcox, B.A., Hahn, G.T., 1965. The effect of strain rate on dislocation multiplication in polycrystalline molybdenum. *Philos. Mag.* 12, 649–653.
<https://doi.org/10.1080/14786436508218904>
- Gu, Y., El-awady, J.A., 2018. Quantifying the effect of hydrogen on dislocation dynamics : A three-dimensional discrete dislocation dynamics framework. *J. Mech. Phys. Solids* 112, 491–507.
<https://doi.org/10.1016/j.jmps.2018.01.006>
- Hachet, G., Metsue, A., Oudriss, A., Feaugas, X., 2018. Influence of hydrogen on the elastic properties of nickel single crystal : A numerical and experimental investigation. *Acta Mater.* 148, 280–288. <https://doi.org/10.1016/j.actamat.2018.01.056>
- Hassan, H., Govind, K., Hartmaier, A., 2018. Micromechanical modelling of coupled crystal plasticity and hydrogen diffusion. *Philos. Mag.* 0, 1–24.
<https://doi.org/10.1080/14786435.2018.1530466>
- Itakura, M., Kaburaki, H., Yamaguchi, M., Okita, T., 2013. The effect of hydrogen atoms on the screw dislocation mobility in bcc iron : A first-principles study. *Acta Mater.* 61, 6857–6867.
<https://doi.org/10.1016/j.actamat.2013.07.064>
- Johnson, W.H., 1875. On some remarkable change produced in iron and steel by the action of hydrogen and acids, *Proceedings of the Royal Society of London* 23, 168-179 (1875). *Proc. R. Soc. A Math. Phys. Eng. Sci.* 179, 1875. <https://doi.org/https://doi.org/10.1098/rspl.1874.0024>
- Jun, D., Hao-nan, Z., Lu-sheng, W., Xia, H., Jian, W., Kun, S., Shi-qing, L., Xiang-guo, Z., 2018. Influence of loading directions on dislocation slip mechanism of nanotwinned Ni with void defect at the twin boundary. *Comput. Mater. Sci.* 152, 1–11.
<https://doi.org/10.1016/j.commatsci.2018.05.026>
- Krom, A.H.M., Koers, R.W.J., Bakker, A., 1999. Hydrogen transport near a blunting crack tip. *J. Mech. Phys. Solids* 47, 971–992. [https://doi.org/10.1016/S0022-5096\(98\)00064-7](https://doi.org/10.1016/S0022-5096(98)00064-7)
- Kubin, L.P., Estrin, Y., 1991. Dynamic strain ageing and the mechanical response of alloys. *J. Phys.* III 1, 929–943. <https://doi.org/10.1051/jp3:1991166>

- Kumnick, A.J., Johnson, H.H., 1980. Deep trapping states for hydrogen in deformed iron. *Acta Metall.* 28, 33–39. [https://doi.org/10.1016/0001-6160\(80\)90038-3](https://doi.org/10.1016/0001-6160(80)90038-3)
- Kwon, Y.J., Seo, H.J., Kim, J.N., Lee, C.S., 2018. Effect of grain boundary engineering on hydrogen embrittlement in Fe-Mn-C TWIP steel at various strain rates. *Corros. Sci.* 142, 213–221. <https://doi.org/10.1016/j.corsci.2018.07.028>
- Li, J., Oudriss, A., Metsue, A., Bouhattate, J., Feaugas, X., 2017. Anisotropy of hydrogen diffusion in nickel single crystals: the effects of self-stress and hydrogen concentration on diffusion. *Sci. Rep.* 7, 45041. <https://doi.org/10.1038/srep45041>
- Liu, Q., Hansen, N., 1995. Deformation Microstructure and Orientation of fcc crystals. *phys. stat. sol.* 187, 187–199.
- Lu, G., Zhang, Q., Kioussis, N., Kaxiras, E., 2001. Hydrogen-Enhanced Local Plasticity in Aluminum : An Ab Initio Study 1–4. <https://doi.org/10.1103/PhysRevLett.87.095501>
- Lu, Q., You, Z., Huang, X., Hansen, N., Lu, L., 2017. Dependence of dislocation structure on orientation and slip systems in highly oriented nanotwinned Cu. *Acta Mater.* 127, 85–97. <https://doi.org/10.1016/j.actamat.2017.01.016>
- Lynch, S.P., 2011. Hydrogen embrittlement (HE) phenomena and mechanisms. *Stress Corros. Crack. Theory Pract.* 30, 90–130. <https://doi.org/10.1533/9780857093769.1.90>
- Ma, A., Hartmaier, A., 2014. On the influence of isotropic and kinematic hardening caused by strain gradients on the deformation behaviour of polycrystals. *Philos. Mag.* 94, 125–140. <https://doi.org/10.1080/14786435.2013.847290>
- Magnin, T., Bosch, C., Wolski, K., Delafosse, D., 2001. Cyclic plastic deformation behaviour of Ni single crystals oriented for single slip as a function of hydrogen content. *Mater. Sci. Eng. A* 314, 7–11. [https://doi.org/10.1016/S0921-5093\(00\)01920-1](https://doi.org/10.1016/S0921-5093(00)01920-1)
- Martínez-Pañeda, E., Del Busto, S., Niordson, C.F., Betegon, C., 2016a. Strain gradient plasticity modeling of hydrogen diffusion to the crack tip. *Int. J. Hydrogen Energy* 41, 10265–10274. <https://doi.org/10.1016/j.ijhydene.2016.05.014>
- Martínez-Pañeda, E., Niordson, C.F., Gangloff, R.P., 2016b. Strain gradient plasticity-based modeling of hydrogen environment assisted cracking. *Acta Mater.* 117, 321–332. <https://doi.org/10.1016/j.actamat.2016.07.022>
- Mecking, H., Kocks, U.F., 1981. Kinetics of flow and strain-hardening. *Acta Metall.* 29, 1865–1875. [https://doi.org/10.1016/0001-6160\(81\)90112-7](https://doi.org/10.1016/0001-6160(81)90112-7)
- Meissonnier, F.T., Busso, E.P., Dowd, N.P.O., 2001. Finite element implementation of a generalised non-local rate-dependent crystallographic formulation for finite strains 17, 601–640. [https://doi.org/10.1016/S0749-6419\(00\)00064-4](https://doi.org/10.1016/S0749-6419(00)00064-4)
- Momotani, Y., Shibata, A., Terada, D., Tsuji, N., 2017. Effect of strain rate on hydrogen embrittlement in low-carbon martensitic steel. *Int. J. Hydrogen Energy* 42, 3371–3379. <https://doi.org/10.1016/j.ijhydene.2016.09.188>
- Murakami, Y., Matsuoka, S., 2010. Effect of hydrogen on fatigue crack growth of metals. *Eng. Fract. Mech.* 77, 1926–1940. <https://doi.org/10.1016/j.engfracmech.2010.04.012>
- Nagumo, M., Nakamura M., T.K., 2001. Hydrogen thermal desorption relevant to delayed-fracture susceptibility of high strength steels 32, 339–347. <https://doi.org/10.1007/s11661-001-0265-9>
- Novak, P., Yuan, R., Somerday, B.P., Sofronis, P., Ritchie, R.O., 2010. A statistical, physical-based, micro-mechanical model of hydrogen-induced intergranular fracture in steel. *J. Mech.*

- Phys. Solids 58, 206–226. <https://doi.org/https://doi.org/10.1016/j.jmps.2009.10.005>
- Nye, J.F., 1953. Some geometrical relations in dislocated crystals. *Acta Metall.* 1, 153–162. [https://doi.org/https://doi.org/10.1016/0001-6160\(53\)90054-6](https://doi.org/https://doi.org/10.1016/0001-6160(53)90054-6)
- Oriani R.A., 1972. A Mechanistic Theory of Hydrogen Embrittlement of Steels. *Technol. Asp.* 76, 848–857. <https://doi.org/https://doi.org/10.1002/bbpc.19720760864>
- Oriani R.A., 1970. The diffusion and trapping of hydrogen in steel. *Acta Metall.* 18, 147–157. [https://doi.org/https://doi.org/10.1016/0001-6160\(70\)90078-7](https://doi.org/https://doi.org/10.1016/0001-6160(70)90078-7)
- Oudriss, A., Creus, J., Bouhattate, J., Conforto, E., Berziou, C., Savall, C., Feaugas, X., 2012a. Grain size and grain-boundary effects on diffusion and trapping of hydrogen in pure nickel. *Acta Mater.* 60, 6814–6828. <https://doi.org/10.1016/j.actamat.2012.09.004>
- Oudriss, A., Creus, J., Bouhattate, J., Savall, C., Peraudeau, B., Feaugas, X., 2012b. The diffusion and trapping of hydrogen along the grain boundaries in polycrystalline nickel. *Scr. Mater.* 66, 37–40. <https://doi.org/10.1016/j.scriptamat.2011.09.036>
- Park, C., Kang, N., Liu, S., 2017. Effect of grain size on the resistance to hydrogen embrittlement of API 2W Grade 60 steels using in situ slow-strain-rate testing. *Corros. Sci.* 128, 33–41. <https://doi.org/10.1016/j.corsci.2017.08.032>
- Paxton, A.T., Katzarov, I.H., 2016. Quantum and isotope effects on hydrogen diffusion, trapping and escape in iron. *Acta Mater.* 103, 71–76. <https://doi.org/10.1016/j.actamat.2015.09.054>
- Paxton, A.T., Sutton, A.P., Finnis, M.W., 2017. The challenges of hydrogen and metals. *Philos. Trans. R. Soc. A* 375. <https://doi.org/10.1098/rsta.2017.0198>
- Pressouyre, G.M., 1979. A classification of hydrogen traps in steel. *Metall. Trans. A* 10, 1571–1573. <https://doi.org/10.1007/BF02812023>
- Robertson, I.M., Sofronis, P., Nagao, A., Martin, M.L., Wang, S., Gross, D.W., Nygren, K.E., 2015. Hydrogen Embrittlement Understood. *Metall. Mater. Trans. A Phys. Metall. Mater. Sci.* 46, 2323–2341. <https://doi.org/https://doi.org/10.1007/s11663-015-0325-y>
- Schwaiger, R., Moser, B., Dao, M., Chollacoop, N., Suresh, S., 2003. Some critical experiments on the strain-rate sensitivity of nanocrystalline nickel. *Acta Mater.* 51, 5159–5172. [https://doi.org/10.1016/S1359-6454\(03\)00365-3](https://doi.org/10.1016/S1359-6454(03)00365-3)
- Singh, R., Singh, A., Singh, P.K., Mahajan, D.K., 2019. Role of prior austenite grain boundaries in short fatigue crack growth in hydrogen charged RPV steel. *Int. J. Press. Vessel. Pip.* 171, 242–252. <https://doi.org/10.1016/j.ijpvp.2019.03.004>
- Sofronis, P., McMeeking, R.M., 1989. Numerical analysis of hydrogen transport near a blunting crack tip. *J. Mech. Phys. Solids* 37, 217–350. [https://doi.org/https://doi.org/10.1016/0022-5096\(89\)90002-1](https://doi.org/https://doi.org/10.1016/0022-5096(89)90002-1)
- Song, J., Curtin, W.A., 2014. Mechanisms of hydrogen-enhanced localized plasticity : An atomistic study using a -Fe as a model system. *Acta Mater.* 68, 61–69. <https://doi.org/10.1016/j.actamat.2014.01.008>
- Song, J., Curtin, W.A., 2012. Atomic mechanism and prediction of hydrogen embrittlement in iron. *Nat. Mater.* 12, 145–151. <https://doi.org/10.1038/nmat3479>
- Takasawa, K., Ikeda, R., Ishikawa, N., Ishigaki, R., 2011. Effects of grain size and dislocation density on the susceptibility to high-pressure hydrogen environment embrittlement of high-strength low-alloy steels. *Int. J. Hydrogen Energy* 37, 2669–2675. <https://doi.org/10.1016/j.ijhydene.2011.10.099>

- Tehranchi, A., Curtin, W.A., 2019. The role of atomistic simulations in probing hydrogen effects on plasticity and embrittlement in metals. *Eng. Fract. Mech.* 106502. <https://doi.org/10.1016/j.engfracmech.2019.106502>
- Tehranchi, A., Curtin, W.A., 2017. Atomistic study of hydrogen embrittlement of grain boundaries in nickel: I. Fracture. *J. Mech. Phys. Solids* 101, 150–165. <https://doi.org/10.1016/j.jmps.2017.01.020>
- Wang, S., Hashimoto, N., Ohnuki, S., 2013. Hydrogen-induced change in core structures of $\{110\}[111]$ edge and $\{110\}[111]$ screw dislocations in iron. *Sci. Rep.* 3, 10–13. <https://doi.org/10.1038/srep02760>
- Wen, M., Zhang, L., An, B., Fukuyama, S., Yokogawa, K., 2009. Hydrogen-enhanced dislocation activity and vacancy formation during nanoindentation of nickel. *Phys. Rev. B - Condens. Matter Mater. Phys.* 80, 1–5. <https://doi.org/10.1103/PhysRevB.80.094113>
- Xie, D., Li, S., Li, M., Wang, Z., Gumbsch, P., Sun, J., Ma, E., Li, J., Shan, Z., 2016. Hydrogenated vacancies lock dislocations in aluminium. *Nat. Commun.* 7, 13341. <https://doi.org/10.1038/ncomms13341>
- Yu, H., Cocks, A., Tarleton, E., 2018. Discrete dislocation plasticity HELPs understand hydrogen effects in bcc materials 0, 1–20. <https://doi.org/10.1016/j.jmps.2018.08.020>
- Zan, N., Ding, H., Guo, X., Tang, Z., Bleck, W., 2015. Effects of grain size on hydrogen embrittlement in a Fe-22Mn-0.6C TWIP steel. *Int. J. Hydrogen Energy* 40, 10687–10696. <https://doi.org/10.1016/j.ijhydene.2015.06.112>
- Zhou, G., Zhou, F., Zhao, X., Zhang, W., Chen, N., Wan, F., Chu, W., 1998. Molecular dynamics simulation of hydrogen enhancing dislocation emission. *Sci. China* 41, 176–181.